JOURNAL OF PETROLOGY | VOLUME 54 | NUMBER 12 | PAGES 2547–2580 | 2013 | doi:10.1093/petrology/egt056

Building of the Deep Gangdese Arc, South Tibet: Paleocene Plutonism and Granulite-Facies Metamorphism

ZEMING ZHANG[1]*, XIN DONG[1], HUA XIANG[1], J. G. LIOU[2] AND M. SANTOSH[3,4]

[1]INSTITUTE OF GEOLOGY, CHINESE ACADEMY OF GEOLOGICAL SCIENCE, NO. 26 BAIWANZHUANG ROAD, BEIJING 100037, CHINA

[2]DEPARTMENT OF GEOLOGICAL AND ENVIRONMENTAL SCIENCES, STANFORD UNIVERSITY, STANFORD, CA 94305, USA

[3]DIVISION OF INTERDISCIPLINARY SCIENCE, FACULTY OF SCIENCE, KOCHI UNIVERSITY, AKEBONO-CHO, KOCHI 780-8520, JAPAN

[4]SCHOOL OF EARTH SCIENCE AND RESOURCES, CHINA UNIVERSITY OF GEOSCIENCES BEIJING, BEIJING 100083, CHINA

RECEIVED DECEMBER 10, 2012; ACCEPTED AUGUST 5, 2013
ADVANCE ACCESS PUBLICATION OCTOBER 16, 2013

The Nyingchi complex, forming the eastern segment of the Gangdese magmatic arc, occurs within the southern Lhasa terrane in south Tibet, and is composed dominantly of plutons and their metamorphosed equivalents. Together with some metasedimentary units these rocks record multiple Mesozoic and Cenozoic magmatic and metamorphic events during northward subduction of Neo-Tethyan oceanic lithosphere beneath the Eurasian continent. Petrological and geochronological studies reveal that the Nyingchi complex experienced intense Paleocene subduction-related magmatism and almost synchronous granulite-facies metamorphism accompanied by the formation of S-type granites. Subduction-related I-type granitoids show geochemical features typical of continental magmatic arcs; zircon separates from them yield $^{206}Pb/^{238}U$ ages from c. *65 to* c. *56 Ma, and commonly display positive $\varepsilon_{Hf}(t)$ values ranging from −1·7 to +13·0. The occurrence of magmatic epidote, as well as the syn-intrusion high-grade metamorphism, indicates that the plutons were emplaced at middle to lower crustal depths within the Lhasa terrane. Associated S-type granitoids are peraluminous and contain garnet and muscovite; their zircons yield $^{206}Pb/^{238}U$ ages ranging from* c. *66 to* c. *55 Ma, and these have distinct but mostly negative $\varepsilon_{Hf}(t)$ values from −18·4 to +2·1. The zircons from the associated metasedimentary rocks include both detrital and metamorphic types; the detrital zircons yielded variable inherited $^{206}Pb/^{238}U$ ages ranging from* c. *2910 to* c. *235 Ma, constraining the maximum depositional age to the Triassic. The metamorphic zircons from the metaplutonic and metasedimentary rocks yielded ages from* c. *67 to 52 Ma. Phase equilibria modeling shows that the Nyingchi complex experienced peak granulite-facies metamorphism and partial melting under conditions of 800–830°C and 9–10·5 kbar, and then cooled isobarically to* c. *700°C in the lower crust at depths of >30 km. We argue that rollback of the flat-subducted Neo-Tethyan oceanic slab during Early Paleogene times resulted in a contractional orogeny and intrusion of voluminous mantle-derived magmas, which caused large-scale crustal heating, partial melting and granulite-facies metamorphism within the deep crust of the Gangdese arc. The Nyingchi complex represents the exposed lower crust of the Gangdese magmatic arc, and links the granulite-facies metamorphism with silicic magmatism and crustal growth during Paleocene arc accretion.*

KEY WORDS: *Gangdese magmatic arc; crustal growth; granulite; S-type granite; south Tibet*

*Corresponding author. Telephone: 86-10-68999735. Fax: 86-10-68994781. E-mail: zzm2111@sina.com

INTRODUCTION

The present-day formation of new continental crust is, in general, attributed to magmatic processes at active continental margins and within intra-plate settings (Jagoutz *et al.*, 2007). Nearly 80–95% of the post-Archean continental crust is considered to have formed by processes similar to those taking place in present-day subduction zones (Taylor & McLennan, 1985; Schubert & Sandwell, 1989; Rudnick, 1995; Barth *et al.*, 2000; Daczko *et al.*, 2002; Garrido *et al.*, 2006; Dhuime *et al.*, 2007, 2009; Jagoutz *et al.*, 2007). Therefore, investigations on subduction zone processes provide important clues to understanding the formation of the continental crust. Although magmatic intrusive rocks in upper and middle crustal sections have been extensively studied, our understanding of crust formation is hampered by the scarcity of data concerning deep crustal processes. Accordingly, understanding deep-seated magmatism and metamorphism in active continental margins is crucial to evaluate continent building processes (e.g. Cawthorn & O'Hara, 1976; Taylor & McLennan, 1985; Hildreth & Moorbath, 1988; Rudnick, 1995; Müntener *et al.*, 2000; Jagoutz *et al.*, 2007, 2011; Jagoutz & Schmidt, 2012).

As part of the Himalayan–Tibetan orogen, the southern Lhasa Terrane has been widely accepted as a Mesozoic Andean-type convergent margin associated with the northward subduction of Neo-Tethyan oceanic lithosphere and an archetype of a Cenozoic collisional orogen related to India–Asia collision (Allègre *et al.*, 1984; Coulon *et al.*, 1986; Yin & Harrison, 2000; Mo *et al.*, 2005; Aitchison *et al.*, 2011; Xia *et al.*, 2011; Pan, G. T., *et al.*, 2012; Zhang & Santosh, 2012; Zhu *et al.*, 2012). To better understand the complex orogenesis, most previous studies have focused on the Mesozoic and Cenozoic magmatic rocks in this region, which form huge, multiple volcanic–plutonic arcs, cored by the Kohistan–Ladakh and Gangdese (Trans-Himalayan) batholiths (e.g. Honegger *et al.*, 1982; Burg & Chen, 1984; Schärer *et al.*, 1984; Debon *et al.*, 1986; Harris *et al.*, 1988; Weinberg & Dunlap, 2000; Rolland *et al.*, 2002; Schaltegger *et al.*, 2002; Bignold & Treloar, 2003; Chung *et al.*, 2003, 2005, 2009; Ding *et al.*, 2003; Hou *et al.*, 2004, 2009; Mo *et al.*, 2005, 2007, 2008; Chu *et al.*, 2006; Heuberger *et al.*, 2007; Singh *et al.*, 2007; Upadhyay *et al.*, 2008; Ji *et al.*, 2009; Ravikant *et al.*, 2009; Zhao *et al.*, 2009; Zhu *et al.*, 2009*a*, 2009*b*, 2009*c*, 2011*b*; Zhang *et al.*, 2010*b*; Pan, F. B., *et al.*, 2012). In contrast, the high-grade metamorphic rocks formed within the deep crust of the Gangdese arc have received much less attention (Harris *et al.*, 1988; Wallis *et al.*, 2003; Dong *et al.*, 2010*b*, 2011*a*, 2011*b*; Searle *et al.*, 2010; Zhang *et al.*, 2010*a*, 2013).

The Nyingchi complex at the Eastern Himalayan syntaxis is well exposed, owing to rapid Late Cenozoic uplift and erosion, and comprises high-grade metamorphic rocks and associated plutonic rocks within the southeastern Lhasa terrane (Burg *et al.*, 1997; Zhang *et al.*, 2010*a*; Guo *et al.*, 2012; Xu *et al.*, 2012, 2013). These rocks provide a window into the middle to lower crust of the Gangdese magmatic arc (Searle *et al.*, 2011; Zhang *et al.*, 2013). In this study, we present new petrological, geochemical and geochronological data for granulite-facies metamorphic rocks and associated plutons to constrain processes operating in the lower crust of the Gangdese arc during Paleocene times, and to establish the link between granulite-facies metamorphism and magmatism during accretionary orogeny. Our results contribute to a better understanding of crustal growth and evolution in an active continental margin tectonic setting.

GEOLOGICAL SETTING

The Himalayan orogen of south Tibet is composed essentially of the Himalayan sequences and south Lhasa terrane, separated by the Indus–Yarlung Tsangpo suture zone, representing the remnants of the Neo-Tethyan Ocean (Fig. 1) (Yin & Harrison, 2000; Yin, 2006, and references therein). In the eastern Himalayan syntaxis, the Himalayan sequences include the Tethys–Himalayan sequence and the High Himalayan crystalline sequence. The former consists of low-grade metasedimentary rocks and Paleozoic to Mesozoic sedimentary strata. The High Himalayan rocks crop out in the middle part of the syntaxis, and consist of high-pressure (HP) granulite-facies metamorphic rocks with variable protolith ages, referred to as the Namche Barwa complex (Zhang *et al.*, 2012*b*, and references therein).

The Lhasa terrane, located in the northern part of Himalayan orogen, is a large crustal segment (Fig. 1), speculated to have rifted from Gondwana in Triassic or Middle to Late Jurassic times and drifted northward before colliding with Eurasia along the Bangong–Nujiang suture zone in the Cretaceous. An Andean-type active continental margin has also been proposed in the southern part of the terrane prior to its collision with the northward moving Indian continent in the Cenozoic (e.g. Yin & Harrison, 2000; Wu *et al.*, 2010; Hebert *et al.*, 2012; Chatterjee *et al.*, 2013, and references therein).

Previous studies considered the Lhasa terrane to be composed dominantly of Precambrian crystalline basement, Paleozoic to Mesozoic marine strata and arc-type volcanic rocks, together with Mesozoic and Cenozoic intrusions (e.g. Yin & Harrison, 2000; Pan *et al.*, 2004, 2006). The southern segment of the Lhasa terrane is dominated by the Cretaceous–Tertiary Gangdese batholith and the Paleogene Linzizong volcanic succession, with minor Triassic–Cretaceous volcano-sedimentary rocks (Pan *et al.*, 2004, 2006; Zhu *et al.*, 2008, 2012). The Gangdese batholith consists of a wide range of lithologies ranging from gabbro, diorite and granodiorite to granite. Geochemically these rocks are comparable with I-type granitoids such as those from the Cordilleran regions in

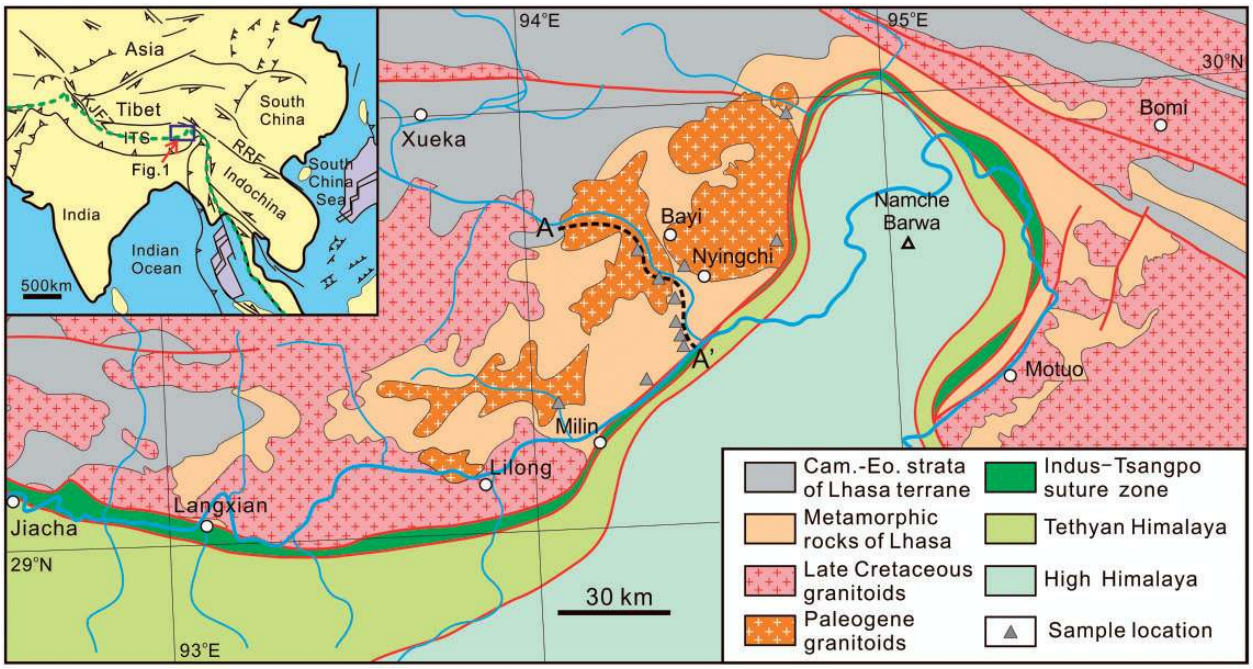

Fig. 1. Schematic geological map of the Eastern Himalayan Syntaxis (EHS), showing the study area and line of section A–A' in Fig. 2 and sample locations. ITS, Indus–Tsangpo Suture; KJFS, Karakorum–Jiali Fault Zone; RRF, Red River Fault.

the circum-Pacific orogen and have Sr and Nd isotope compositions indicative of significant involvement of a juvenile mantle source in magma generation (Harris *et al.*, 1988; Mo *et al.*, 2005, 2008; Chu *et al.*, 2006; Wen *et al.*, 2008*a*, 2008*b*; Zhu *et al.*, 2011*a*, 2011*b*, 2012). The Gangdese batholith has been dated as Late Triassic to Miocene (~205–9 Ma; Chu *et al.*, 2006; Wen *et al.*, 2008*b*; Chung *et al.*, 2009; Ji *et al.*, 2009; Zhu *et al.*, 2011*b*), with four discrete stages of magmatic activity, ~205–152 Ma, ~109–80 Ma, ~65–41 Ma and ~33–13 Ma, respectively, with the 65–41 Ma stage being the most prominent (Mo *et al.*, 2005; Wen *et al.*, 2008*b*; Ji *et al.*, 2009). In addition, several Early Paleozoic and Late Devonian to Carboniferous granites have recently been recognized in the eastern part of the southern Lhasa terrane (Dong *et al.*, 2010*a*, 2010*b*; Ji *et al.*, 2012).

Numerous medium- to high-grade metamorphic rocks occur in the southeastern part of the Lhasa terrane, especially in the east and west domains of the Eastern Himalayan Syntaxis (EHS), which swings northward into the Lhasa terrane (Fig. 1). Traditionally, the metamorphic rocks on the east side of the EHS were termed the Bomi Group and those on the west the Nyingchi Group, with a general correlation with the Precambrian metamorphic basement of the Lhasa terrane (e.g. Pan *et al.*, 2004, 2006; Yin *et al.*, 2006). However, recent laser ablation inductively coupled plasma mass spectrometry (LA-ICP-MS) and sensitive high-resolution ion microprobe (SHRIMP) zircon U–Pb *in situ* dating has revealed that these rocks experienced Late Mesozoic to early Cenozoic metamorphism (Dong *et al.*, 2010*a*, 2010*b*; Zhang *et al.*, 2010*b*; Guo *et al.*, 2011, 2012; Zhang & Wu, 2012; Xu *et al.*, 2013). Inherited detrital zircons from the metasedimentary rocks yield a wide range of U–Pb ages from ~3300 to ~250 Ma, and the meta-intrusions have various protolith ages including Ordovician (~496 Ma), Devonian (~360 Ma), Cretaceous (~90 Ma) and Eocene (~55 Ma) (Dong *et al.*, 2010*a*, 2010*b*; Zhang *et al.*, 2010*a*, 2013; Zhang & Wu, 2012; Guo *et al.*, 2012). The protoliths of these metamorphic rocks, termed the Nyingchi complex in this study, thus include sedimentary and igneous rocks of various ages.

The western part of the Eastern Himalayan syntaxis in our study area is composed of Gangdese batholiths and their metamorphosed equivalents with a compositionally variable intrusive suite of gabbroic diorite, diorite, granodiorite, granite and leucogranite (Figs 1 and 2). Granitoids occur as batholiths, stocks, dikes and veins; most intrusive dikes of various sizes parallel the nearly vertical foliation of the high-grade metamorphic rocks (Fig. 2b). These granitoids have a massive structure, or show various degrees of deformation and metamorphic foliation (Fig. 2e–g). The granitoids have a wide range of crystallization ages from 120 to 20 Ma and most exhibit intrusive relationships between the various phases (Fig. 2g).

The metasedimentary units in the study area are dominantly composed of pelitic schists, paragneisses and amphibolites, with minor quartzite, calc-silicate rocks and

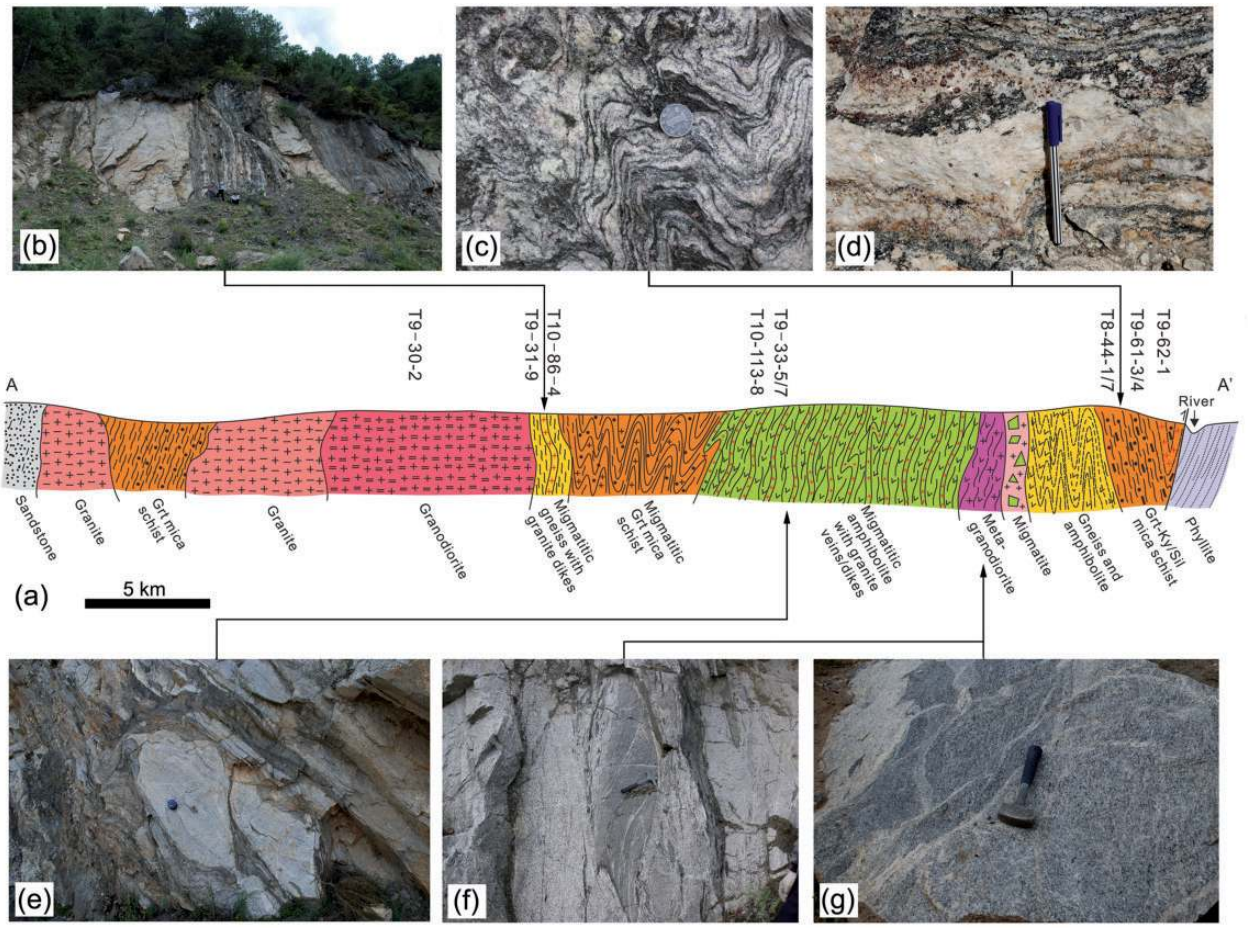

Fig. 2. (a) Cross-section, and (b–g) field photographs of Nyingchi granite, leucogranite (garnet-bearing two-mica granite), granodiorite and gabbroic diorite, migmatitic garnet–sillimanite mica schist, garnet–kyanite mica schist, gneiss and amphibolite, migmatite. The (A) and (A′) ends of the profile in (a) are Carboniferous meta-sandstone of the Lhasa terrane and phyllite of the Indus–Tsangpo suture zone respectively. (b) Granite dikes parallel to the nearly vertical foliation of migmatitic amphibolite with abundant felsic veins, suggesting anatexis. (c) Garnet–sillimanite mica schist with abundant anatectic veins, which has experienced intensive deformation. Both host-rock and vein contain pink garnet. (d) Anatectic veins within the garnet–sillimanite mica schist consist of feldspar, quartz and variable amounts of garnet and muscovite. (e) Metagranodiorite lens within gneiss and amphibolite layers; all rocks exhibit intensive deformation and migmatization. (f) Metagranodiorite with lenses of migmatitic amphibolite. (g) Metagranodiorite (right side) intruded into intensively deformed and metamorphosed gabbroic diorite (centre left), and subsequently intruded by undeformed granite (left).

marble. These rocks underwent intense deformation and granulite-facies metamorphism, resulting in partial melting and migmatization (Fig. 2); some contain abundant anatectic veins, including felsic, leucogranitic and pegmatitic veins (Fig. 2). The most pronounced ones are garnet- and muscovite-bearing leucogranite veins, which resulted from partial melting of sillimanite- or kyanite-bearing garnet–mica schists (Fig. 2c and d).

ANALYTICAL METHODS

The mineral compositions of the studied rocks were analyzed using a JEOL JXA 8900 electron microprobe (EPM) and a 15 kV accelerating voltage, 5 nA beam current, 5 μm probe diameter, and count time of 10 s for peak and background, at the State Key Laboratory of Continental Tectonics and Geodynamics, Institute of Geology, Chinese Academy of Geological Science. Natural or synthetic standards were used for EPM analysis and ZAF corrections were carried out.

Whole-rock compositions were analyzed at the National Geological Analysis Center of China, Beijing. Oxides of major elements, including loss on ignition (LOI), were determined by X-ray fluorescence (XRF) (Rigaku-3080) with an analytical uncertainty of <0·5%. Trace elements Zr, Nb, V, Cr, Sr, Ba, Zn, Ni, Rb and Y were analyzed using a different XRF instrument (Rigaku-2100) with an analytical uncertainty of <3–5%. Other trace elements and rare earth elements (REE) were analyzed by ICP-MS (TJA-PQ-ExCell); analytical uncertainties are 1–5% when the abundance is greater than 1 ppm, and 5–10% when the abundance is less than 1 ppm.

Zircon U–Pb dating and trace element analysis were simultaneously conducted by LA-ICP-MS at the State Key Laboratory of Geological Processes and Mineral Resources, China University of Geosciences. Detailed operating conditions for the laser ablation system and the ICP-MS instrument are as described by Liu *et al.* (2008, 2010). Laser sampling was conducted using an Excimer 193 nm GeoLas 2005 System with a spot size of 32 μm. An Agilent 7500a ICP-MS instrument was used to acquire ion-signal intensities. Nitrogen was introduced into the central gas flow (Ar + He) of the Ar plasma in the LA-ICP-MS analysis, which increases the sensitivity for most elements by a factor of ~2 compared with the results without adding nitrogen (Hu *et al.*, 2008). To keep time-dependent elemental fractionation at a low level, a laser frequency of 4 Hz and a laser energy of 60 mJ were applied (Zong *et al.*, 2010; Hu *et al.*, 2011). The uncertainty of analysis is within ~1% for the zircon standard.

Zircon 91500 was used as external standard for U–Pb dating, and was analyzed twice every five analyses. Time-dependent drifts of U–Th–Pb isotopic ratios were corrected using a linear interpolation (with time) for every five analyses according to the variations of 91500 (i.e. two zircon 91500 + five samples + two zircon 91500) (Liu *et al.*, 2010). Preferred U–Th–Pb isotopic ratios used for 91500 are from Wiedenbeck *et al.* (1995). Uncertainty in the preferred values for the external standard 91500 was propagated to the ultimate results for the samples. Concordia diagrams and weighted mean calculations were made using Isoplot/Ex.ver3 (Ludwig, 2003). Trace element compositions of zircons were calibrated against multiple-reference materials (BCR-2G and BIR-1G) combined with internal standardization (Liu *et al.*, 2010). The preferred values of element concentrations for the USGS reference glasses used are from the GeoReM database (http://georem.mpch-mainz.gwdg.de/).

In situ Hf isotope compositions of zircon were determined using a Neptune Plus multicollector (MC)-ICP-MS system (Thermo Fisher Scientific, Germany) and a Geolas 2005 Excimer ArF laser ablation system (Lambda Physik, Göttingen, Germany) at the State Key Laboratory of Geological Processes and Mineral Resources, China University of Geosciences, Wuhan. The energy density of laser ablation used was 5·3 J cm^{-2}. Helium was used as the carrier gas in the ablation cell and was merged with argon (makeup gas) after the ablation cell. All data for zircon in this study were acquired in the single-spot ablation mode at a spot size of 32 μm. Each measurement consisted of 20 s of acquisition of the background signal followed by 50 s of ablation signal acquisition. The operating conditions for the laser ablation system and the MC-ICP-MS instrument, and the analytical method, are the same as those described in detail by Hu *et al.* (2012).

PETROLOGY

Petrography

Paleocene granitoids from the study area are classified as I-type granodiorite, diorite and gabbroic diorite, and S-type granite and granodiorite according to their mineral assemblage and whole-rock composition. The metasedimentary rocks are schists and paragneisses. The petrological characteristics of these rocks, including mineralogy, protolith type, magmatic and metamorphic age, and sample locations, are listed in Table 1. Mineral abbreviations are after Whitney & Evans (2010).

Granitoids

The I-type granodiorites consist mainly of plagioclase, quartz and biotite, with minor K-feldspar and epidote. Most magmatic epidotes are subhedral and with an allanite core (Fig. 3a).

The S-type granitoids consist mainly of subhedral microcline, plagioclase, biotite, muscovite and garnet, and anhedral quartz (Fig. 3b and c). In one sample, magmatic garnet occurs as anhedral skeletal grains, intergrown with quartz (Fig. 3c).

Meta-granitoids

Most metamorphosed I-type granitoids have intermediate to mafic compositions. Both meta-diorite (garnet–biotite gneiss) and meta-granodiorite (garnet–biotite gneiss) have similar mineral assemblage of plagioclase, quartz, biotite and garnet. Meta-gabbroic diorite (garnet–biotite–amphibole gneiss) consists of plagioclase, biotite, amphibole and quartz, with or without garnet. The porphyroblastic garnet contains quartz inclusions (Fig. 3d).

Metasedimentary rocks

Schist and paragneiss show clear foliation defined by elongated mica, sillimanite and kyanite. The garnet–kyanite–two-mica schist (T9-61-4) consists of plagioclase, biotite, muscovite, garnet, kyanite and quartz (Fig. 4a and b). The cores of the garnet porphyroblasts contain inclusions of sillimanite, biotite, plagioclase and quartz, whereas the rims have no inclusions (Fig. 4a and b). This texture and the compositional zoning of garnet described below indicate that the schist has two-stage mineral assemblages; that is, the garnet cores and mineral inclusions form an early mineral assemblage of Grt + Sil + Bt + Pl + Qz, and the garnet rims and matrix minerals form a late assemblage of Grt + Ky + Bt + Ms + Pl + Qz. Moreover, both kyanite and biotite are partly replaced by muscovite and plagioclase (Fig. 4a and b), suggesting a late retrogression. Similar zoning relations of garnet porphyroblasts occur in a garnet–two-mica schist (T9-61-3), consisting of Grt + Bi + Pl + Qz + Ms (Fig. 4c); the core has biotite, plagioclase and quartz inclusions, and the rim is inclusion-free. Some pelitic schists from the study area contain abundant

Table 1: The major features of the studied rocks from the Nyingchi complex

Sample	Rock	Protolith or type	Mineral assemblage	Magmatic age (Ma)	Metamorphic age (Ma)	Location
Granitoids or meta-granitoids						
T8-15-2	Ep granodiorite	I-type	Pl, Kf, Bt, Ep, Qz	63·0 ± 0·6		29°17′50″N, 94°00′50″E
T9-30-2	Ep granodiorite	I-type	Pl, Kf, Bt, Ep, Qz	63·2 ± 0·8		29°37′51″N, 94°20′55″E
T9-33-5	Ep granodiorite	I-type	Pl, Kf, Bt, Ep, Qz	64·8 ± 1·3		29°32′54″N, 94°26′14″E
T9-62-1	Grt–Bt gneiss	I-type granodiorite	Pl, Grt, Bt, Qz	63·6 ± 1·8		29°26′00″N, 94°27′10″E
T10-74-1	Grt–Bt gneiss	I-type diorite	Pl, Grt, Bt, Qz	60·2 ± 1·1	61·8 ± 2·4	29°38′11″N, 94°42′45″E
T10-74-2	Grt–Bt–Amp gneiss	I-type gabbroic diorite	Pl, Grt, Bt, Am, Qz	61·3 ± 1·2	59·8 ± 3·3	29°38′11″N, 94°42′45″E
T10-86-4	Bt amphibolite	I-type gabbroic diorite	Pl, Am, Bt, Qz	55·8 ± 5·8	53·1 ± 2·0	29°35′41″N, 94°22′26″E
T10-113-8	Grt two-mica granite	I-type	Pl, Kf, Qz, Grt, Bt, Ms	63·3 ± 0·8		29°32′54″N, 94°26′14″E
T10-123-2	Two-mica granite	S-type	Pl, Kf, Qz, Bt, Ms	61·9 ± 0·4		29°36′20″N, 94°24′24″E
T10-72-2	Grt two-mica granodiorite	S-type	Pl, Grt, Bt, Ms, Qz	65·9 ± 1·1		29°57′24″N, 94°47′17″E
T9-33-7	Grt two-mica granodiorite	S-type	Pl, Kf, Grt, Bt, Ms, Qz	54·9 ± 0·8		29°32′54″N, 94°26′14″E
Metasedimentary rocks						
T8-20-3	Grt–Ms–Qz schist	Graywacke	Grt, Ms, Qz		67·2 ± 1·4	29°17′55″N, 94°15′55″E
T9-31-9	Grt–Cpx–Amp gneiss	Graywacke	Grt, Cpx, Am, Pl, Qz		51·6 ± 0·8	29°35′42″N, 94°22′21″E
T9-61-4	Grt–Ky two-mica schist	Pelitic	Grt, Ky, Ms, Bt, Pl, Qz, Gr			29°26′03″N, 94°27′10″E
T8-44-1	Grt–Sill–Bt schist	Pelitic	Grt, Bt, Sil, Pl, Kfs, Qz, Gr			29°27′58″N, 94°24′58″E
T9-61-3	Grt two-mica schist	Pelitic	Grt, Bt, Ms, Pl, Qz, Gr			29°26′03″N, 94°27′10″E
T8-44-7	Grt–Sill–Bt gneiss	Graywacke	Grt, Bt, Sil, Pl, Kfs, Qz, Gr			29°27′58″N, 94°24′58″E

sillimanite; most sillimanite crystals are replaced by late-stage biotite and muscovite (Fig. 4d). The dated schist (T8-20-3) and paragneiss (T9-31-9) respectively are composed of Ms + Grt + Qz and Pl + Di + Grt + Amp + Qz.

Mineral compositions

The compositions of the major minerals in the granitoids and metamorphic rocks were analyzed by EPMA; representative data are listed in Tables 2–7, and characteristic features are described below.

Amphibole occurs in the amphibolite (meta-gabbroic diorite, T10-86-4), and in the garnet–biotite gneiss (meta-gabbroic diorite, T10-74-2). Analyzed amphiboles have similar SiO_2 (43·3–45·5 wt %), CaO (11·5–11·6 wt %), FeO (16·4–18·2 wt %), Na_2O (1·3–1·5 wt %) and K_2O (0·5–0·7 wt %) contents, and belong to the calcic amphibole group.

Biotite is common in I- and S-type granitoids, orthogneisses and pelitic schists. Biotites from the intrusive rocks has relatively high FeO (20·8–26·0 wt %), and low MgO (6·6–9·5 wt %) and Al_2O_3 (15·1–17·7 wt %) (Table 3), whereas those from the metamorphic rocks have lower FeO (12·6–21·4 wt %) and higher MgO (8·6–13·9 wt %). Most analyzed biotites have high TiO_2 contents (>2·0 wt %).

Minor garnets in the S-type granitoids (Fig. 3c) represent magmatic phase and have high MnO (3·9–12·2 wt %) and low MgO (2·0–3·2 wt %); thus they have high spessartine (9–27%) and low pyrope (8–12%) components (Table 4; Fig. 5). Garnet in both orthogneisses (Fig. 3b) and pelitic schists (Fig. 4) is a major metamorphic phase and has higher MgO (4·7–8·4 wt %) and lower MnO (0·5–3·1 wt %) compared with the magmatic garnet (Table 4; Fig. 5). The garnet grains from the pelitic schists studied exhibit similar compositional zoning (Table 4 and Fig. 6). The porphyroblastic garnet from the garnet–kyanite–two-mica schist (T9-61-4) is characterized by decreasing MgO (8·4 to 6·5 wt %) and MnO, and increasing CaO (1·6 to 3·7 wt %) from core to rim (Fig. 6a). Although FeO varies across the grain core, it increases near the rim and then decreases at the outermost rim. The porphyroblastic garnet grain from the garnet–two-mica schist (T9-61-3) has a wide and homogeneous core, and a very thin rim showing a sharp decrease of MgO (8·20 to 5·64 wt %), and increase of CaO (2·01 to 5·41 wt %) and FeO (Fig. 6b).

Plagioclase is common in both magmatic and metamorphic rocks. Plagioclase from a granite sample has relatively low anorthite contents of 16–21%, whereas that from the granodiorites has a higher anorthite content of

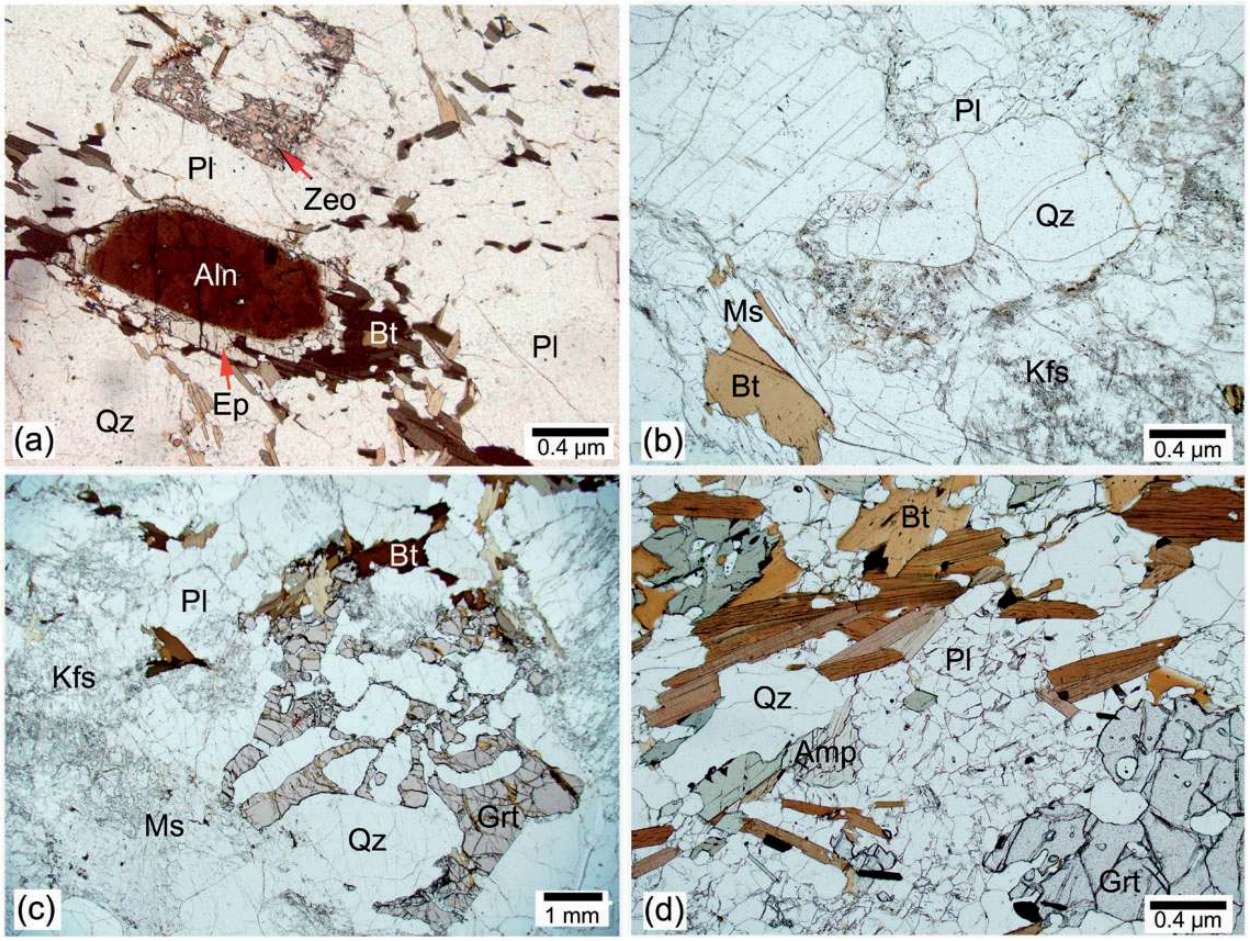

Fig. 3. Photomicrographs of granitoids and gneiss. (a) Epidote-bearing granodiorite (T9-30-2) consists mainly of plagioclase (Pl), quartz (Qz) and biotite (Bt) and epidote (Ep), and shows a granitic texture; the epidote has a core of allanite and the plagioclase is partly replaced by zeolite (Zeo). (b) Two-mica granite (T10-123-2) consists of K-feldspar (Kfs), Pl, Qz, Bt and muscovite (Ms), with a granular texture. (c) Garnet-bearing granodiorite (T10-72-2) contains Pl and Qz, with minor Kfs, Bt, Ms and garnet (Grt), with a granular texture; the garnet forms skeletal crystals and intergrowths with quartz. (d) Garnet–biotite–amphibole gneiss (meta-gabbroic diorite, T10-74-2) consists of Pl, Bt, Qz, Grt and amphibole (Amp) with minor opaque minerals, and has a porphyroblastic texture; the porphyroblastic garnet contains Qz inclusions.

26–39% (Table 5). Plagioclases from the pelitic schists have similar compositions, with anorthite contents of 30–36%; those from the meta-diorite (gneiss) have higher anorthite contents of 42–47%. The plagioclase from the meta-gabbroic diorites has the highest anorthite content of 78–89%.

The magmatic epidotes in the I-type granodiorites have similar compositions, with 13·0–14·0 wt % Fe_2O_3 and 23·3–23·8 wt % CaO (Table 6). They have restricted pistacite (Ps) contents [i.e. atomic $Fe^{3+}/(Fe^{3+}+Al^{3+})$] between 25 and 30%, which are compatible with primary magmatic epidotes reported in Late Cretaceous and Early Cenozoic intrusions from the Gangdese arc (Wen *et al.*, 2008*b*; Zhang, H. F., *et al.*, 2010), and match the chemical criteria of magmatic epidotes (Zen & Hammarstrom, 1984; Schmidt & Poli, 2004). It is noted that some epidotes have low totals, indicating a presence of an REE component, which is consistent with the epidote containing an allanite core.

Magmatic muscovite crystals from three granodiorites have variable compositions with SiO_2 of 44·7–47·3 wt %, Al_2O_3 of 30·0–34·1 wt %, FeO of 1·5–4·8 wt %, MgO of 0·2–1·3 wt % and TiO_2 of 0·0–1·2 wt %. By comparison, metamorphic muscovite from the pelitic schists has higher SiO_2 (47·3–48·3 wt %) and lower FeO (1·1–1·3 wt %) (Table 7). Muscovites from both magmatic and metamorphic rocks have similar Si cations of 3·1–3·2 atoms per formula unit; a.p.f.u.) per 11 oxygens.

WHOLE-ROCK GEOCHEMISTRY

Whole-rock major and trace element compositions of the studied rocks are presented in Tables 8 and 9.

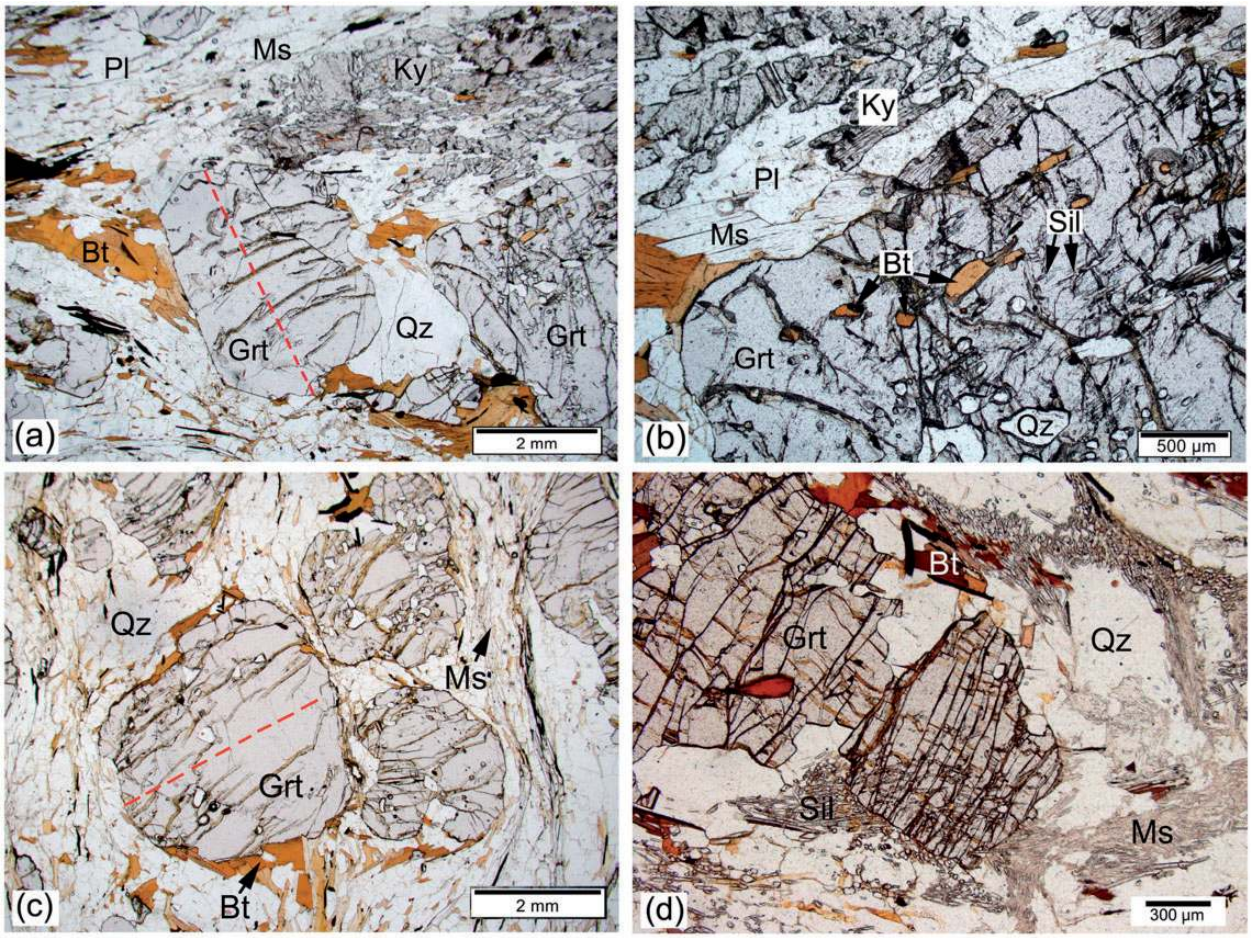

Fig. 4. Photomicrographs of metasedimentary rocks. (a, b) Garnet–kyanite-two mica schist (T9-61-4) consists of Grt, Bt, Ms, Ky, Pl and Qz, with a lepidoblastic texture. The porphyroblastic garnet contains Sil, Qz and Bt inclusions. (c) Garnet-two mica schist (T9-61-3) consists of Grt, Bt, Pl, Qz and Ms. The porphyroblastic garnet cores contain Bt, Pl and Qz inclusions. (d) Garnet–sillimanite biotite schist (T8-44-7); the matrix sillimanite is partly replaced by biotite and muscovite. Red dashed lines crossing the garnet porphyroblasts in (a) and (c) represent the locations of the analyzed compositional profiles.

The Paleocene granitoids exhibit a wide major element compositional range, with SiO_2 55·2–75·6 wt %, Al_2O_3 14·0–18·5 wt %, MgO 0·1–4·2 wt %, total FeO 0·3–9·7 wt %, NaO_2 0·5–4·0 wt % and K_2O 0·9–6·1 wt %. Based on the classification scheme of Middlemost (1994), the I-type granitoids are classified as gabbroic diorite, diorite and granodiorite, whereas the S-type granitoids are granodiorite and granite; both are sub-alkaline except for a K_2O-rich S-type granite, which is alkaline (Fig. 7a). The granitoids have relatively high Al_2O_3 contents and thus high A/CNK values (mostly >1·0), and are peraluminous except for meta-gabbroic diorite sample T10-74-2 with an A/CNK value of 0·98, which is metaluminous (Fig. 7b).

The granitoids have variable trace element compositions with Rb 28–150 ppm, Sr 111–602 ppm and Ba 184–757 ppm (Table 8). Their primitive-mantle normalized multi-element patterns exhibit large ion lithophile element (LILE) enrichment, and Nb, Ta and Ti negative anomalies (Fig. 8a and b). The I-type granitoids have variable but relatively high rare earth element (REE) contents (47–284 ppm, Table 8), and show fractionated REE patterns, characterized by light REE (LREE) enrichment and heavy REE (HREE) depletion, without or with small Eu anomalies (Fig. 8c). However, the S-type granites show distinctly negative Ti anomalies (Fig. 8b), and V-shaped REE patterns with slight HREE enrichment (Fig. 8d). Most granitoids have chemical compositions similar to those of typical arc magmatic rocks, plotting in the field of volcanic arc granites in Nb vs Y and Rb vs Y + Nb diagrams (Fig. 7c and d).

The metasedimentary rocks have highly variable major element compositions, with SiO_2 61·9–79·9 wt %, Al_2O_3 9·6–16·2 wt %, MgO 0·2–3·5 wt %, total FeO 0·6–7·9 wt %, NaO_2 0·2–2·5 wt % and K_2O 0·1–2·6 wt % (Table 9). These rocks also have variable trace element concentrations; most show positive anomalies in Ba, Sr and Zr in

Table 2: The compositions of representative amphiboles from the meta-gabbroic diorites

Rock:	Gneiss				Amphibolite			
Sample:	T10-74-2	T10-74-2	T10-74-2	T10-74-2	T10-86-4	T10-86-4	T10-86-4	T10-86-4
SiO_2	44·55	43·28	45·21	44·84	45·53	44·16	44·46	44·86
TiO_2	0·87	0·85	0·86	0·90	0·64	0·80	0·76	0·80
Al_2O_3	12·78	13·50	11·74	11·82	12·09	13·05	13·00	12·27
Cr_2O_3	0·03	0·00	0·02	0·00	0·02	0·00	0·02	0·00
FeO	17·17	16·45	16·44	16·89	17·02	18·15	17·76	17·39
MnO	0·14	0·04	0·10	0·13	0·39	0·53	0·47	0·60
MgO	9·79	8·90	10·01	10·00	9·01	8·73	8·94	9·18
CaO	11·55	11·58	11·55	11·55	11·49	11·59	11·60	11·58
Na_2O	1·31	1·46	1·26	1·26	1·36	1·43	1·35	1·38
K_2O	0·68	0·64	0·59	0·64	0·59	0·63	0·59	0·54
Total	98·86	96·72	97·80	98·07	98·17	99·07	98·94	98·60
O = 23								
Si	6·409	6·358	6·567	6·505	6·617	6·371	6·414	6·487
Al	2·165	2·335	2·008	2·019	2·069	2·218	2·208	2·089
Cr	0·003	0·000	0·002	0·000	0·002	0·000	0·002	0·000
Fe^{2+}	1·000	0·963	1·083	1·039	1·241	1·040	1·077	1·053
Fe^{3+}	1·066	1·058	0·914	1·010	0·828	1·150	1·066	1·050
Ti	0·094	0·094	0·094	0·098	0·070	0·087	0·082	0·087
Mg	2·100	1·949	2·167	2·163	1·952	1·878	1·923	1·979
Mn	0·017	0·005	0·012	0·016	0·048	0·065	0·057	0·073
Ca	1·781	1·822	1·797	1·796	1·789	1·792	1·793	1·794
Na	0·365	0·416	0·355	0·354	0·383	0·400	0·378	0·387
K	0·125	0·120	0·109	0·118	0·109	0·116	0·109	0·100

mantle-normalized trace element patterns (Fig. 8e). Except for sample T8-20-3, which has a very low REE content and flat REE pattern, the other rocks have relatively high REE contents and LREE-rich and flat HREE patterns (Fig. 8f). Most of the protoliths of these metasedimentary rocks are pelite and greywacke.

PHASE EQUILIBRIA MODELING OF METAMORPHISM

Here we quantitatively estimate the metamorphic conditions of two representative pelitic schists from *P–T* pseudosections and garnet isopleth thermobarometry. The forward modeling using a pseudosection predicts the phase relations depending on bulk-rock composition, which can constrain the mineral reactions during metamorphism and melting, and permit comparisons with the observed phase relation (e.g. Powell *et al.*, 1998). The *P–T* pseudosections were calculated with the PERPLEX computer program package (Connolly, 2005; version of August 2012) and the internally consistent thermodynamic dataset of Holland & Powell (1998, updated 2002). The activity–solution models used in the pseudosection calculations are clino- and orthoamphibole (Diener *et al.*, 2007), clinopyroxene (Green *et al.*, 2007), garnet (White *et al.*, 2007), orthopyroxene, spinel, staurolite, cordierite (Holland & Powell, 1998), biotite (Tajčmanová *et al.*, 2009), white mica (Coggon & Holland, 2002) and feldspar (Fuhrman & Lindsley, 1988).

The *P–T* pseudosections were calculated in the system $MnO–Na_2O–CaO–K_2O–FeO–MgO–TiO_2–Al_2O_3–SiO_2–H_2O$ (MnNCKFMTASH), a system close to the compositions of most natural rocks. The 1·8% H_2O content calculated from the modal amounts of biotite and muscovite is adopted in the modelling of the two samples. Such an H_2O content is normal for high-grade metapelites (White *et al.*, 2007). The value of O, to reflect the oxidation state of the system, was probably very low, as suggested by the absence of Fe^{3+}-rich oxides, and therefore we assume all iron as ferrous. Our modelling shows that although a change in oxidation state may have certain effects on the *P–T* conditions of key metamorphic assemblages and

Table 3: The compositions of representative biotites from the granitoids and metamorphic rocks

Rock:	Granodiorite					Granite	Gneiss		Amphibolite	Schist			
Sample:	T8-15-2	T9-30-2	T9-33-7	T10-72-2	T10-123-2	T10-113-8	T10-74-1	T10-74-2	T10-86-4	T8-44-1	T8-44-7	T9-61-3	T9-61-4
SiO_2	35·82	36·94	35·47	36·25	36·01	36·16	37·20	37·06	37·43	36·14	35·24	38·84	39·24
TiO_2	2·77	2·77	3·14	2·56	3·07	3·19	2·67	2·73	2·40	3·10	4·44	1·90	1·81
Al_2O_3	15·32	16·00	16·72	16·48	17·59	16·58	18·15	15·87	16·21	18·57	17·98	17·75	17·23
Cr_2O_3	0·00	0·02	0·00	0·00	0·01	0·00	0·00	0·02	0·03	0·00	0·03	0·13	0·06
FeO	21·09	22·77	23·01	25·26	22·21	23·76	21·38	19·67	18·32	15·56	16·69	13·65	12·58
MnO	0·74	0·51	0·30	0·20	0·37	0·72	0·13	0·08	0·20	0·03	0·05	0·04	0·01
MgO	9·43	8·19	7·43	6·65	8·09	7·08	8·68	10·68	9·48	11·56	9·43	13·04	13·07
CaO	0·00	0·00	0·00	0·03	0·00	0·00	0·00	0·07	0·30	0·02	0·03	0·05	0·11
Na_2O	0·08	0·07	0·11	0·13	0·20	0·04	0·15	0·21	0·15	0·19	0·18	0·21	0·19
K_2O	9·34	9·36	8·78	9·16	9·19	9·05	9·15	8·63	7·51	9·41	9·35	9·07	8·22
Total	94·60	96·63	94·98	96·72	96·73	96·57	97·52	95·02	92·04	94·65	93·41	94·67	92·50
O = 22													
Si	5·832	5·897	5·765	5·843	5·721	5·804	5·804	5·897	6·060	5·683	5·659	5·995	6·127
Al	2·938	3·008	3·200	3·128	3·291	3·134	3·335	2·974	3·091	3·439	3·400	3·226	3·168
Ti	0·339	0·333	0·384	0·310	0·367	0·385	0·313	0·327	0·292	0·367	0·536	0·221	0·213
Fe^{2+}	2·872	3·040	3·128	3·405	2·951	3·190	2·790	2·618	2·481	2·046	2·242	1·762	1·643
Cr	0·000	0·003	0·000	0·000	0·001	0·000	0·000	0·003	0·004	0·000	0·004	0·016	0·007
Mn	0·102	0·069	0·041	0·027	0·050	0·098	0·017	0·011	0·027	0·004	0·007	0·005	0·001
Mg	2·289	1·949	1·800	1·598	1·916	1·694	2·019	2·534	2·288	2·710	2·258	3·001	3·042
Ca	0·000	0·000	0·000	0·005	0·000	0·000	0·000	0·012	0·052	0·003	0·005	0·008	0·018
Na	0·025	0·022	0·035	0·041	0·062	0·012	0·045	0·065	0·047	0·058	0·056	0·063	0·058
K	1·940	1·906	1·821	1·883	1·863	1·853	1·821	1·752	1·551	1·888	1·916	1·786	1·637

overall topology, the garnet compositional isopleths show no substantial differences. Therefore, the oxidation state has no significant effect on the precise P–T determinations as they are calculated from the garnet compositional isopleths.

The X_{Mg} [= Mg/(Mg + Fe)] and X_{Ca} [= Ca/(Fe + Ca + Mg + Mn)] isopleths were used as two independent thermodynamic variables to describe the compositional variation of garnet in P–T space. The intersections of the isopleths that represent the observed garnet compositions are used for P–T estimates of the respective increment of garnet growth. This approach (i.e. garnet isopleth thermobarometry) has been widely applied in estimating P–T paths from garnet zoning, even in the case where the equilibrium compositions of coexisting minerals are uncertain (e.g. Tinkham & Ghent, 2005; Gaidies *et al.*, 2006; Wei & Song, 2008; Burenjargal *et al.*, 2012).

The calculated P–T pseudosection for garnet–kyanite–two-mica schist (T9-61-4) shows that garnet, biotite and plagioclase are stable in the calculated P–T range of 650–850°C and 4–14 kbar (Fig. 9). Cordierite appears at lower pressures (<6–7 kbar). The solidus of the system is located at $T = 650$–725°C, with a negative slope; the muscovite-out reaction occurs at *c.* 720–810°C above *c.* 9·5 kbar. The volume fraction of melt increases with increasing temperature (Fig. 9a). The observed matrix assemblage of Grt + Bt + Ms + Pl + Ky + Qz + melt is stable in a P–T field of 690–760°C and 9–12·5 kbar (the blue field in Fig. 9), and the early inclusion assemblage of Grt + Bt + Sil + Pl + Qz + melt is in a P–T field of 720–850°C and 7–10·5 kbar (the yellow field in Fig. 9).

The calculated garnet composition isopleths are shown in Fig. 9b. The X_{Mg} value increases with increasing temperature, whereas the X_{Ca} value (grossular content) increases with increasing pressure and decreasing temperature. As described above, garnet from the schist preserves compositional zoning (Table 4 and Fig. 6a). For the garnet core, the composition isopleths of $X_{Mg} = 0{\cdot}33$–$0{\cdot}34$ and $X_{Ca} = 0{\cdot}04$–$0{\cdot}05$ (Table 4) intersect exactly at the upper stability field of the observed early mineral assemblage, indicating metamorphic P–T conditions of 800–820°C and 9–10 kbar (the red-filled circle in Fig. 9).

Table 4: The compositions of representative garnets from the granitoids and metamorphic rocks

Rock:	Granodiorite				Granite		Schist							
Sample:	T9-33-7		T10-72-2		T10-113-8		T9-61-4							
Domain:							Rim	Rim	Core	Core	Core	Core	Rim	Rim
SiO_2	37·27	37·16	37·58	37·67	37·25	37·66	37·93	38·74	38·76	38·53	37·68	38·49	38·91	38·79
TiO_2	0·00	0·00	0·05	0·00	0·00	0·00	0·00	0·00	0·03	0·00	0·03	0·05	0·00	0·00
Al_2O_3	20·60	20·46	20·52	20·23	20·44	20·37	21·07	21·11	21·26	21·16	21·34	20·91	21·04	20·91
Cr_2O_3	0·00	0·00	0·00	0·00	0·06	0·02	0·07	0·00	0·01	0·03	0·04	0·00	0·01	0·06
FeO	30·79	31·86	31·73	31·78	26·13	26·27	28·80	29·48	29·19	29·39	29·82	29·41	29·52	29·43
MnO	4·31	3·94	3·91	4·13	12·23	11·98	0·69	0·92	0·61	0·68	0·58	0·59	0·98	0·91
MgO	2·49	2·72	3·15	3·09	1·99	1·99	5·59	7·18	8·36	8·18	8·07	7·90	7·25	5·77
CaO	4·82	4·78	4·65	4·73	2·79	2·86	5·14	2·43	1·67	1·62	1·64	1·70	2·38	4·09
Total	100·29	100·91	101·63	101·63	100·92	101·16	99·30	99·87	99·91	99·59	99·22	99·07	100·08	99·97
O = 12														
Si	2·996	2·980	2·985	2·996	3·002	3·022	2·994	3·027	3·009	3·005	2·952	3·022	3·034	3·042
Ti	0·000	0·000	0·003	0·000	0·000	0·000	0·000	0·000	0·002	0·000	0·002	0·003	0·000	0·000
Al	1·953	1·934	1·922	1·897	1·942	1·928	1·960	1·945	1·946	1·945	1·970	1·935	1·934	1·933
Cr	0·000	0·000	0·000	0·000	0·004	0·002	0·004	0·000	0·001	0·002	0·003	0·000	0·001	0·004
Fe^{3+}	0·081	0·157	0·150	0·166	0·082	0·039	0·051	0·002	0·032	0·043	0·122	0·019	0·000	0·000
Fe^{2+}	1·990	1·979	1·958	1·949	1·679	1·724	1·851	1·924	1·864	1·874	1·832	1·912	1·925	1·930
Mn	0·294	0·267	0·263	0·278	0·834	0·814	0·046	0·061	0·040	0·045	0·038	0·039	0·064	0·060
Mg	0·299	0·325	0·373	0·366	0·239	0·238	0·657	0·837	0·968	0·951	0·942	0·925	0·843	0·675
Ca	0·415	0·411	0·395	0·403	0·241	0·246	0·435	0·203	0·139	0·135	0·138	0·143	0·199	0·344
Cations	8·027	8·053	8·051	8·056	8·028	8·013	7·997	7·999	8·000	8·000	7·998	7·997	7·999	7·988
Alm	0·67	0·68	0·67	0·67	0·57	0·58	0·62	0·64	0·62	0·62	0·62	0·63	0·64	0·64
Spe	0·10	0·09	0·08	0·09	0·27	0·27	0·02	0·02	0·01	0·01	0·01	0·01	0·02	0·02
Prp	0·10	0·10	0·12	0·12	0·08	0·08	0·22	0·28	0·32	0·32	0·32	0·31	0·28	0·22
Grs	0·13	0·13	0·13	0·13	0·08	0·08	0·15	0·07	0·05	0·04	0·05	0·05	0·07	0·11

(continued)

For the garnet inner rim (excluding the outermost two spots), the composition isopleths of $X_{Mg} = 0{\cdot}30$ and $X_{Ca} = 0{\cdot}07$ intersect at a P–T condition of *c.* 770°C and *c.* 10·5 kbar (the yellow-filled circle in Fig. 9). For the outermost rim of garnet, the X_{Mg} value decreases to 0·26, passing to the lower stability field of the observed matrix mineral assemblage (the blue field in Fig. 9). Thus the garnet–kyanite–two-mica schist probably underwent peak-stage granulite-facies metamorphism at P–T conditions of 800–820°C and 9–10 kbar, followed by a near-isobaric cooling process constrained by the connecting of the P–T estimates of the garnet core, inner rim and outer rim (Fig. 9). This modelling indicates that melt generation in the pelitic schist occurred via muscovite dehydration melting (Ms + Pl + Qz = Sil + Kfs + melt); the maximum melt modal content is 18–20% of the whole-rock volume during the peak-metamorphism (Fig. 9a).

The P–T pseudosection for the garnet mica schist (T9-61-3) indicates that garnet and plagioclase are all stable in the calculated P–T range of 660–900°C and 5–14 kbar (Fig. 10). Biotite disappears at high temperature (>850°C) and low pressure (<6 kbar). Cordierite appears at lower pressure (<7 kbar). The solidus of the system is located at $T = 650$–730°C, and the muscovite-out reaction including kyanite occurs at *c.* 710–800°C above *c.* 9 kbar. The volume fraction of melt increases with increasing temperature (Fig. 10a). The observed matrix assemblage Grt + Bt + Pl + Ms + Qz + melt is stable at 670–725°C and 10·5–14 kbar (the blue field in Fig. 10), whereas the garnet core and its inclusion mineral assemblage (Grt + Bt + Pl + Ms + Qz + melt) yields a wide P–T field of *c.* 720–900°C and 6–10·5 kbar (the yellow field in Fig. 10).

The calculated garnet composition isopleths are shown in Fig. 10b. The X_{Mg} values increase with increasing

Table 4: Continued

Rock:	Schist												Gneiss	
Sample:	T9-61-3										T8-44-7		T10-74-2	
Domain:	Rim	Rim	Rim	Core	Core	Core	Core	Rim	Rim	Rim				
SiO_2	38·28	38·52	38·21	39·22	39·11	38·94	38·59	38·58	37·96	38·07	38·28	37·32	38·24	38·35
TiO_2	0·01	0·02	0·01	0·01	0·00	0·02	0·04	0·01	0·03	0·00	0·00	0·00	0·00	0·00
Al_2O_3	21·00	21·00	21·01	21·25	21·31	21·16	21·34	21·16	21·21	20·94	21·27	21·12	21·06	20·83
Cr_2O_3	0·05	0·03	0·23	0·04	0·00	0·04	0·00	0·08	0·06	0·03	0·03	0·01	0·01	0·00
FeO	28·94	29·71	29·79	28·12	28·06	28·29	28·44	29·93	30·08	29·73	33·96	33·85	31·21	31·94
MnO	0·27	0·45	0·57	1·41	1·39	1·41	1·41	0·49	0·46	0·36	1·39	1·50	0·84	0·87
MgO	5·64	6·46	6·81	8·25	8·25	8·33	8·20	6·91	6·65	5·97	5·84	5·68	4·81	4·69
CaO	5·41	3·66	2·69	2·01	1·99	2·00	2·01	2·43	2·62	4·25	1·51	1·50	5·14	5·17
Total	99·64	99·87	99·33	100·31	100·14	100·19	100·02	99·60	99·09	99·35	102·34	101·09	101·37	101·92
O = 12														
Si	3·009	3·019	3·008	3·032	3·028	3·014	2·994	3·025	2·997	3·004	2·980	2·952	2·995	2·998
Ti	0·001	0·001	0·000	0·000	0·000	0·001	0·002	0·000	0·002	0·000	0·000	0·000	0·000	0·000
Al	1·946	1·939	1·950	1·936	1·944	1·930	1·951	1·956	1·974	1·947	1·952	1·970	1·944	1·919
Cr	0·003	0·002	0·014	0·003	0·000	0·003	0·000	0·005	0·004	0·002	0·002	0·001	0·000	0·000
Fe^{3+}	0·038	0·019	0·021	0·000	0·004	0·038	0·057	0·000	0·025	0·042	0·133	0·192	0·103	0·126
Fe^{2+}	1·864	1·928	1·941	1·818	1·813	1·793	1·788	1·963	1·961	1·919	2·078	2·047	1·941	1·962
Mn	0·018	0·030	0·038	0·092	0·091	0·093	0·092	0·033	0·031	0·024	0·092	0·101	0·056	0·058
Mg	0·661	0·755	0·800	0·951	0·952	0·961	0·949	0·807	0·783	0·702	0·677	0·670	0·561	0·546
Ca	0·455	0·307	0·227	0·167	0·165	0·165	0·167	0·204	0·222	0·359	0·126	0·127	0·431	0·433
Cations	7·994	8·000	7·998	7·999	7·997	7·999	8·000	7·992	7·999	8·000	8·045	8·065	8·035	8·042
Alm	0·62	0·64	0·65	0·60	0·60	0·60	0·60	0·65	0·65	0·64	0·71	0·71	0·66	0·67
Spe	0·01	0·01	0·01	0·03	0·03	0·03	0·03	0·01	0·01	0·01	0·03	0·03	0·02	0·02
Prp	0·22	0·25	0·27	0·31	0·32	0·32	0·32	0·27	0·26	0·23	0·22	0·21	0·18	0·17
Grs	0·15	0·10	0·08	0·06	0·05	0·05	0·06	0·07	0·07	0·12	0·04	0·04	0·14	0·14

temperature, and X_{Ca} values increase with increasing pressure and decreasing temperature. For the garnet core, the isopleths of $X_{Mg} = 0{\cdot}34$–$0{\cdot}35$ and $X_{Ca} = 0{\cdot}05$–$0{\cdot}06$ intersect at the upper stability field of the observed early mineral assemblage, indicating metamorphic P–T conditions of *c.* 810–830°C and 9·5–10 kbar (the red-filled circle in Fig. 10). For the garnet inner rim (excluding the outermost two spots), the isopleths of $X_{Mg} = 0{\cdot}28$–$0{\cdot}29$ and $X_{Ca} = 0{\cdot}07$–$0{\cdot}10$ intersect in a P–T field of *c.* 720–740°C and 10–11·5 kbar (the yellow-filled circle in Fig. 10), which is transitional between the stability fields of three kyanite-bearing mineral assemblages. For the outermost rim of garnet, the X_{Mg} (0·26) and X_{Ca} (0·12–0·15) isopleths intersect in the stability field of the observed matrix mineral assemblage (the blue field in Fig. 10), suggesting a lower metamorphic temperature of *c.* 700°C. Thus, the modeling indicates that the garnet–mica schist underwent the peak-stage metamorphism at P–T conditions of 810–830°C and 9·9–10·5 kbar, and subsequent near-isobaric cooling, as constrained by connecting the P–T conditions of the garnet core, inner rim and outer rim (Fig. 10). Partial melting in the schist occurred via the muscovite-dehydration melting; the maximum melt modal content is 18–20% of the whole-rock volume during the peak-metamorphism (Fig. 10a).

In summary, phase equilibrium modelling shows that the pelitic schists with and without kyanite and sillimanite experienced similar peak-stage granulite-facies metamorphism and intensive anatexis under high-temperature (800–830°C) and high-pressure (9–10·5 kbar) conditions, followed by a similar, near-isobaric, cooling process (Figs 9 and 10). This indicates that the metasedimentary rocks of the Nyingchi complex have been buried at lower crustal depths of >30 km at relatively high geothermal gradients of *c.* 21–25°C km^{-1}.

Table 5: The compositions of representative plagioclases from the granitoids and metamorphic rocks

Rock:	Granodiorite				Granite	Schist		Gneiss		Amphibolite
Sample:	T8-15-2	T9-30-5	T9-33-5	T10-123-2	T10-113-8	T9-61-3	T9-61-4	T10-74-1	T10-74-2	T10-86-4
SiO_2	60·81	61·81	60·89	60·33	63·61	60·43	59·70	57·57	46·94	48·67
Al_2O_3	23·12	23·83	24·50	23·95	22·45	25·04	25·65	26·36	33·45	32·09
FeO	0·00	0·07	0·01	0·01	0·00	0·05		0·01	0·10	0·05
CaO	5·68	5·93	6·93	6·91	4·49	5·90	6·69	9·29	17·88	16·64
Na_2O	8·71	8·56	7·90	7·71	9·24	7·49	7·19	6·47	1·50	2·27
K_2O	0·21	0·21	0·16	0·14	0·36	0·09	0·07	0·11	0·01	0·03
Total	98·57	100·45	100·40	99·09	100·22	99·04	99·32	99·81	99·93	99·82
Si	2·732	2·730	2·701	2·715	2·808	2·723	2·686	2·587	2·162	2·236
Al	1·224	1·240	1·281	1·270	1·168	1·330	1·360	1·396	1·816	1·738
Fe^{3+}	0·081	0·044	0·006	0·000	0·025	0·000	0·000	0·000	0·000	0·000
Ca	0·273	0·281	0·329	0·333	0·212	0·285	0·322	0·447	0·882	0·819
Na	0·758	0·733	0·680	0·673	0·791	0·654	0·627	0·564	0·134	0·202
K	0·012	0·012	0·009	0·008	0·020	0·005	0·004	0·006	0·000	0·002
Ab	0·73	0·71	0·67	0·66	0·77	0·69	0·66	0·55	0·13	0·20
An	0·26	0·27	0·32	0·33	0·21	0·30	0·34	0·44	0·87	0·80
Or	0·01	0·01	0·01	0·01	0·02	0·01	0·00	0·01	0·00	0·00

ZIRCON U–Pb AGE, TRACE ELEMENT AND Hf ISOTOPE DATA

Zircon U–Pb age

LA-ICP-MS U–Pb dating and the trace element compositions of the magmatic and metamorphic zircons and inherited zircons from the granitoids and metasedimentary rocks are presented in Electronic Appendix Tables 1 and 2 (available for downloading at http://www.petrology.oxfordjournals.org), and are described below.

Zircons from the granitoids are commonly colorless, euhedral to subhedral prismatic, and characterized by regular concentric zoning in cathodoluminescence (CL) images (Fig. 11a). Most of the grains have relatively high Th/U ratios (>0·2) and REE contents (Electronic Appendix Table 1), and exhibit fractionated REE patterns with LREE depletion and HREE enrichment, and negative Eu anomalies (Fig. 12a). The internal structure and compositional features indicate that the zircons from the granitoids are of magmatic origin (e.g. Rubatto, 2002). For zircons from two granites and six granodiorites, most of the analytical spots yielded consistent, concordant or near-concordant $^{206}Pb/^{238}U$ ages, with weighted mean ages of *c.* 66–55 Ma (Figs 13 and 14a, b).

Zircons from the meta-granitoids are colorless and subhedral prismatic; they are characterized by well-preserved core–rim zoning structures (Fig. 11b and c). The inherited magmatic cores exhibit oscillatory or banded zoning in CL images, and have relatively high Th/U ratios, high REE contents and distinctly fractionated REE patterns with negative Eu anomalies (Fig. 12b and c). In contrast, the metamorphic rims of the zircons show no zoning (Fig. 11b and c), and have relatively low Th/U ratios and REE contents, and fractionated REE patterns with slightly negative Eu anomalies (Fig. 12b and c), typical of metamorphic origin (Rubatto, 2002). The magmatic cores of zircons from one meta-diorite and two meta-gabbroic diorites yielded near-concordant $^{206}Pb/^{238}U$ ages, with weighted mean ages of $60{\cdot}2 \pm 1{\cdot}1$ Ma, $61{\cdot}3 \pm 1{\cdot}2$ Ma and $55{\cdot}5 \pm 5{\cdot}8$ Ma (Fig. 14c–e), respectively. The metamorphic rims of zircon from these three samples yielded near-concordant $^{206}Pb/^{238}U$ ages, and with weighted mean ages of $61{\cdot}8 \pm 2{\cdot}4$ Ma, $59{\cdot}8 \pm 3{\cdot}3$ Ma and $53{\cdot}1 \pm 2{\cdot}0$ Ma, respectively (Fig. 14c–e). Thus, the magmatic and metamorphic ages are nearly consistent within error for each sample, indicating a close temporal association of magmatism and metamorphism.

Zircons from the garnet-bearing quartz schist (sample T8-20-3) are transparent and subhedral, short or long prismatic in shape, and show patchy zoning (Fig. 11d). They have very low Th/U ratios (<0·01) and LREE contents (Electronic Appendix Table 1), and variable HREE

Table 6: The compositions of representative epidotes from the granodiorites

Sample:	T8-15-2	T8-15-2	T8-15-2	T8-15-2	T9-30-2	T9-30-2	T9-30-2	T9-30-2
SiO_2	36·62	36·90	37·12	37·28	37·90	38·97	38·56	38·57
TiO_2	0·17	0·08	0·06	0·10	0·00	0·05	0·06	0·05
Al_2O_3	22·25	22·52	22·48	22·66	23·15	22·88	22·99	23·16
Cr_2O_3	0·03	0·06	0·02	0·03	0·00	0·00	0·03	0·00
FeO	12·27	12·62	12·53	12·27	11·67	11·84	12·31	12·22
MnO	0·61	0·41	0·48	0·60	0·30	0·31	0·30	0·35
MgO	0·01	0·02	0·04	0·00	0·01	0·01	0·01	0·03
CaO	23·42	23·31	23·40	23·38	23·69	23·61	23·76	23·63
Total	95·43	95·93	96·14	96·35	96·71	97·67	98·03	98·02
O = 12								
Si	2·963	2·968	2·979	2·985	3·013	3·073	3·031	3·032
Ti	0·010	0·005	0·003	0·006	0·000	0·003	0·004	0·003
Al	2·122	2·135	2·126	2·139	2·169	2·127	2·130	2·146
Cr	0·002	0·004	0·001	0·002	0·000	0·000	0·002	0·000
Fe^{3+}	0·930	0·917	0·910	0·875	0·809	0·721	0·798	0·783
Fe^{2+}	0·000	0·000	0·000	0·000	0·000	0·060	0·011	0·020
Mn	0·041	0·028	0·033	0·041	0·020	0·021	0·020	0·023
Mg	0·001	0·002	0·005	0·000	0·001	0·001	0·002	0·004
Ca	2·030	2·009	2·011	2·005	2·018	1·994	2·001	1·990

Some epidotes have low totals because of the potential REE components.

contents (Fig. 12d). The zircons with high HREE concentrations exhibit a smooth increase in normalized values from Gd to Lu, presumably suggesting formation prior to garnet crystallization, whereas the zircons with low HREE contents show relatively flat HREE patterns, demonstrating coeval formation with garnet (Schaltegger *et al.*, 1999; Rubatto, 2002; Wu *et al.*, 2008, 2009). These zircons yielded consistent and near-concordant $^{206}Pb/^{238}U$ ages with a weighted mean age of 67·2 ± 1·4 Ma (Fig. 14f), representing the timing of metamorphism of the host-rock. Zircons from a garnet-bearing gneiss (T9-31-9) are subhedral, short prismatic and exhibit patchy zoning or are unzoned. Thirteen analytical spots yielded concordant $^{206}Pb/^{238}U$ ages with a weighted mean age of 51·6 ± 0·9 Ma (Fig. 15a). These spots have relatively low REE contents and nearly flat HREE patterns with weakly negative Eu anomalies (Fig. 12d), and low Th/U ratios (0·007–0·019; Electronic Appendix Table 1), typical of metamorphic zircon grown in equilibrium with garnet (e.g. Rubatto, 2002).

Zircons from a pelitic schist and a paragneiss are transparent, oval or sub-rounded in shape. Most display a very thin and incomplete metamorphic rim and a large inherited detrital core (Fig. 11e and f). The detrital cores show weak concentric or banded zoning; they have relatively high Th/U ratios and REE contents (Electronic Appendix Table 2), typical of magmatic origin. The detrital zircon cores from two samples yielded variable $^{206}Pb/^{238}U$ ages ranging from 235 to 2518 Ma, and from 250 to 2910 Ma, respectively (Fig. 15b and c; Electronic Appendix Table 2), with three major age populations at *c.* 1020, *c.* 580 and *c.* 330 Ma (Fig. 13d), indicating that the metasedimentary rocks have a maximum deposition age during the Triassic, and were sourced from multiple provenances similar to the Mesozoic sedimentary rocks of the Lhasa terrane (Gehrels *et al.*, 2011).

In summary, zircon U–Pb dating reveals that the Nyingchi complex experienced Early Paleogene magmatism and metamorphism. The magmatism resulted in the generation of the plutonic suite, whereas nearly coeval granulite-facies metamorphism affected both the intrusive and sedimentary units. Our results also suggest that the Early Paleogene tectonothermal events within the Gangdese arc may have been sustained for over 10 Myr.

Zircon Hf isotopes

Among 168 magmatic zircon grains from 11 granitoids dated in this study, 143 were analyzed for their Hf isotope ratios (Electronic Appendix Table 3). Zircons from four S-type granites show variable but mostly negative $\varepsilon_{Hf}(t)$ values ranging from −18·4 to +2·1 (Fig. 16). Zircons from seven I-type granitoids yielded variable but mostly positive

Table 7: The compositions of representative muscovites from the granitoids and metamorphic rocks

Rock:	Granodiorite				Schist		
Sample:	T8-15-2	T9-33-7	T10-72-2	T10-123-2	T9-61-3	T9-61-4	T9-61-4
SiO_2	45·06	46·67	46·23	47·06	47·65	47·87	47·68
TiO_2	0·39	1·14	0·00	1·12	1·11	0·95	1·15
Al_2O_3	30·03	31·29	33·77	33·46	31·93	32·00	32·40
Cr_2O_3	0·00	0·02	0·00	0·00	0·13	0·02	0·08
FeO	4·59	2·96	2·11	1·51	1·14	1·28	1·15
MnO	0·00	0·03	0·05	0·04	0·02	0·02	0·03
MgO	1·33	0·99	0·37	0·73	1·31	1·40	1·28
CaO	0·01	0·06	0·00	0·00	0·01	0·04	0·00
Na_2O	0·31	0·32	0·35	0·50	0·93	0·89	0·80
K_2O	10·37	10·04	10·58	10·02	9·81	9·55	9·62
Total	92·09	93·50	93·47	94·43	94·04	94·02	94·18
O = 10							
Si	3·123	3·166	3·138	3·148	3·207	3·208	3·190
Ti	0·020	0·058	0·000	0·056	0·056	0·048	0·058
Al	2·453	2·502	2·702	2·637	2·533	2·527	2·555
Cr	0·000	0·001	0·000	0·000	0·007	0·001	0·004
Fe^{3+}	0·301	0·136	0·058	0·034	0·000	0·027	0·020
Fe^{2+}	0·000	0·032	0·062	0·050	0·096	0·045	0·045
Mn	0·000	0·002	0·003	0·002	0·001	0·001	0·002
Mg	0·138	0·100	0·038	0·072	0·131	0·140	0·128
Ca	0·000	0·004	0·000	0·000	0·001	0·003	0·000
Na	0·042	0·042	0·046	0·064	0·121	0·115	0·104
K	0·916	0·869	0·917	0·855	0·843	0·817	0·821

$\varepsilon_{Hf}(t)$ values, with a range of −1·7 to +13·0 (Fig. 16). The zircons from the S-type granites have old Hf isotope crustal model ages ($T_{DM}C$) ranging from *c.* 1001 Ma to *c.* 2302 Ma (mostly >1570 Ma), whereas those from the I-type granitoids display distinctly younger model ages of *c.* 305 Ma to *c.* 1241 Ma (mostly <980 Ma).

DISCUSSION

Paleocene magmatism of the Gangdese arc

Our study shows that the Paleocene granitoids from the Nyingchi complex include gabbroic diorite, diorite, granodiorite and granite. All the granitoids exhibit strong subduction-related signatures, including (1) calc-alkaline and metaluminous or slightly peraluminous compositions, (2) negative Nb, Ta and Ti anomalies in multi-element plots (Fig. 8a and b), (3) weakly fractionated REE patterns (Fig. 8c and d), (4) relatively low Y, Nb and Rb contents, limiting the granitoids to the volcanic arc field (Fig. 7c and d). These features are consistent with previous studies that concluded that the Gangdese granitoids are dominated by calc-alkaline I-type magmatic rocks, representing a major component of an Andean-type continental margin that resulted from northward subduction of Neo-Tethyan oceanic lithosphere prior to the India–Eurasia collision (e.g. Allègre *et al.*, 1984; Debon *et al.*, 1986; Searle *et al.*, 1987; Harris *et al.*, 1988; Yin & Harrison, 2000; Chung *et al.*, 2005; Kapp *et al.*, 2005*a*; Mo *et al.*, 2005; Wen *et al.*, 2008*b*).

Previous studies have indicated that S-type granitoids within the Himalayan orogen are younger than *c.* 50 Ma, and related to post-collision crustal thickening (Chung *et al.*, 2005; Mo *et al.*, 2005; Wen *et al.*, 2008*b*; Zhang, H. F., *et al.*, 2010; Searle *et al.*, 2011; Pullen *et al.*, 2011; Zeng *et al.*, 2011). However, our study clearly demonstrates the occurrence of Paleocene S-type granites in the Gangdese arc. These S-type granites are light coloured, commonly termed leucogranite, and occur as veins or dikes with variable widths (Fig. 2b). They are characterized by the presence of aluminous minerals such as garnet and muscovite, and have peraluminous bulk composition. Most zircons from these granites contain inherited detrital cores, indicating that they were derived from metasedimentary rocks or older granite provenances.

A key requisite in S-type granite generation is a metasedimentary source buried in the deep crust before anatexis; some previous investigators have preferred continent–continent collision to explain this (e.g. Barbarin, 1998). However, S-type granites occur sporadically in Phanerozoic circum-Pacific accretionary orogens (Kemp *et al.*, 2007; Collins & Richards, 2008). In addition, Tulloch *et al.* (2009) reported a mid-Paleozoic S-type granite in an active margin of east Gondwana in western New Zealand.

Considering that most granites are crust-derived, the positive and negative $\varepsilon_{Hf}(t)$ values of their zircons would indicate that they originate by partial melting of juvenile and ancient crust, respectively (Kinny & Maas, 2003). Available studies show positive zircon $\varepsilon_{Hf}(t)$ values for the Gangdese granitoids (Fig. 16), suggesting a juvenile source (Chu *et al.*, 2006; Zhang *et al.*, 2007; Chiu *et al.*, 2009; Ji *et al.*, 2009; Zhu *et al.*, 2011*b*). Our study shows that zircons from the Paleocene granitoids of the eastern Gangdese arc have both positive and negative $\varepsilon_{Hf}(t)$ values (Fig. 16). Most zircons from the S-type granites have negative $\varepsilon_{Hf}(t)$ values of up to −18·4, with old Hf isotope crustal model ages ($T_{DM}C$) ranging from 1001 to 2302 Ma (Fig. 16 and Electronic Appendix Table 2). Guo *et al.* (2012) reported a Paleogene (64·4 ± 0·7 Ma) S-type granite from the Nyingchi complex. Inherited zircon cores from the S-type granites have a similar age spectrum to those of the Nyingchi paragneisses; the magmatic zircon rims have distinctly negative $\varepsilon_{Hf}(t)$ values of −17·7 to −8·3,

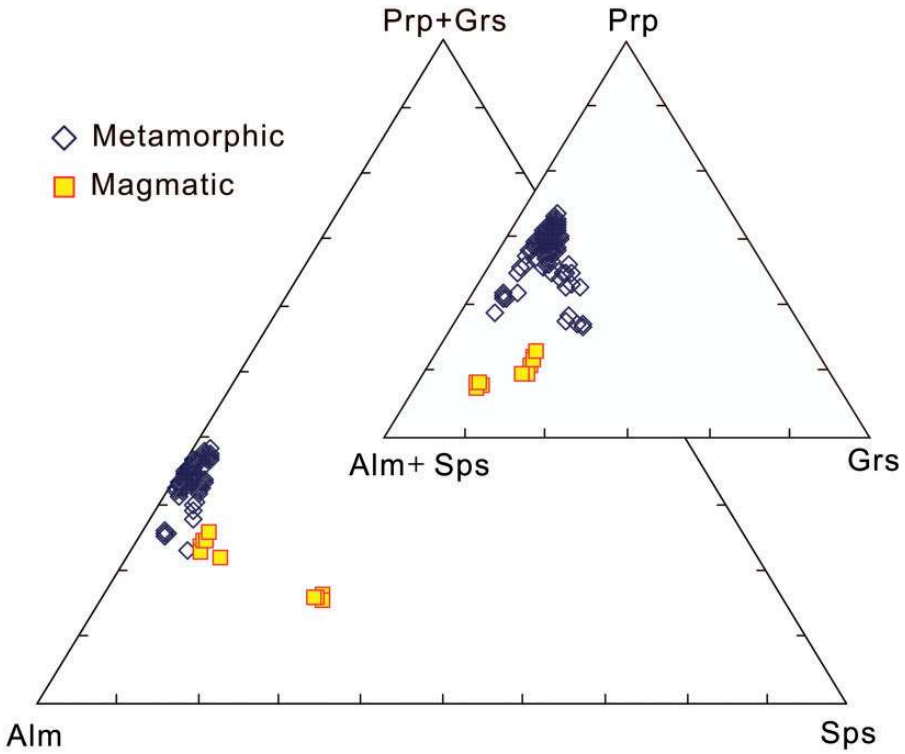

Fig. 5. Compositions of garnets from the magmatic and metamorphic rocks.

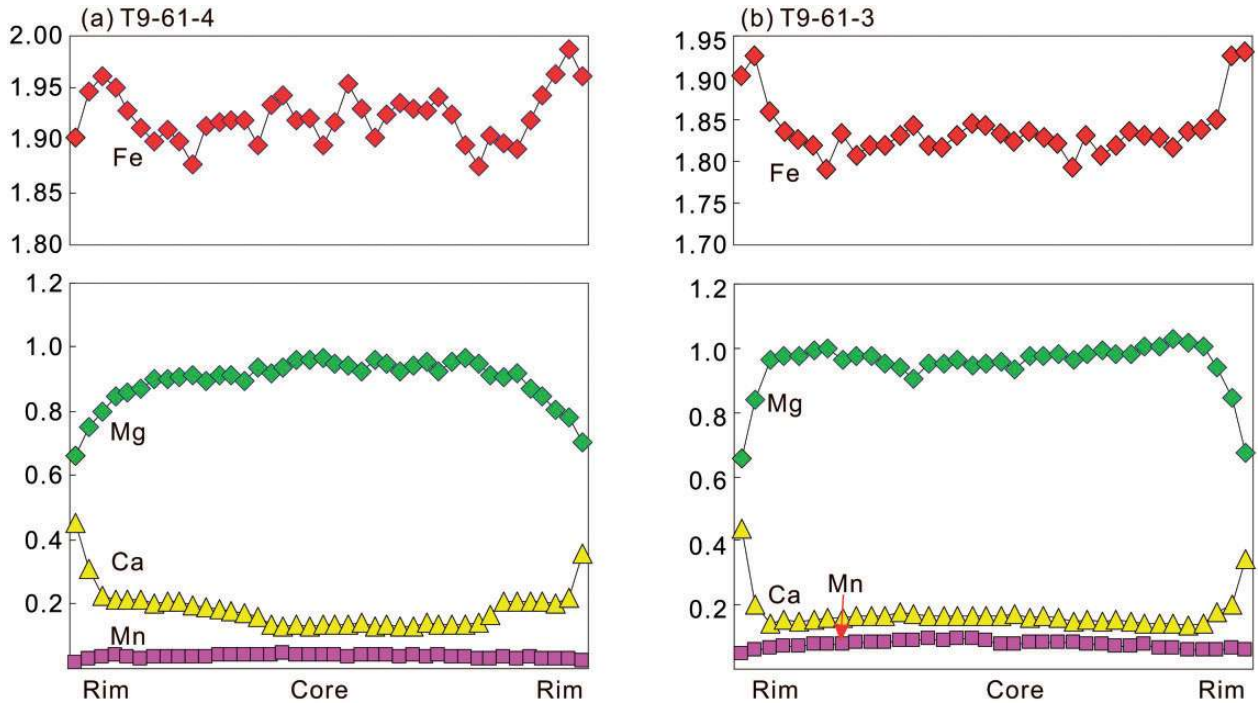

Fig. 6. Garnet compositional profiles (red dashed lines in Fig. 4a and c) representing rim-to-rim analyses through garnet porphyroblasts: (a) T9-61-4; (b) T9-61-3.

Table 8: The whole-rock chemical compositions of the granitoids and metagranitoids from the eastern Gangdese arc

Type:	I-type granitoids							S-type granitoids			
Rock	Granodiorite			Gneiss			Amphibolite	Granite		Granodiorite	
Sample:	T8-15-2	T9-30-2	T9-33-5	T9-62-1	T10-74-1	T10-74-2	T10-86-4	T10-113-8	T10-123-2	T10-72-2	T9-33-7
Major elements (wt %)											
SiO_2	70·46	64·41	68·42	64·27	58·68	55·24	55·22	72·21	75·57	68·34	69·31
TiO_2	0·34	0·65	0·63	0·68	0·94	1·38	1·03	0·04	0·09	0·45	0·39
Al_2O_3	14·32	16·72	15·19	17·25	18·29	18·49	17·62	15·74	13·99	15·46	16·62
Fe_2O_3	1·06	1·15	0·63	0·73	3·22	3·95	3·16	0·08	0·18	1·74	0·26
FeO	2·23	3·32	3·75	4·28	4·42	6·18	5·51	0·27	0·27	3·07	2·07
MnO	0·09	0·09	0·16	0·07	0·17	0·19	0·17	0·06	0·01	0·29	0·06
MgO	1·33	1·57	1·22	2·05	2·20	3·26	4·17	0·11	0·20	1·19	0·66
CaO	3·16	3·87	3·34	4·62	4·92	7·01	7·29	1·17	1·73	3·68	5·73
Na_2O	3·71	3·86	3·98	3·73	3·16	0·53	1·03	3·79	2·55	3·49	2·74
K_2O	2·53	2·56	1·78	1·74	2·40	1·91	2·31	6·09	4·63	1·83	0·89
P_2O_5	0·13	0·22	0·22	0·19	0·64	0·37	0·25	0·04	0·05	0·14	0·10
H_2O	0·49	0·90	0·66	0·45	1·26	1·40	1·06	0·30	0·28	0·42	1·00
LOI	0·74	0·59	0·48	0·35	0·42	0·68	1·07	0·12	0·33	0·41	0·97
Total	100·10	99·01	99·80	99·96	99·46	99·19	98·83	99·72	99·60	100·09	99·80
Trace elements (ppm)											
Hf	7·72	3·70	3·79	2·23	3·84	2·50	3·94	2·76	0·46	5·04	5·19
Zr	94	146	163	80	150	84	151	54	12	187	228
V	57·1	67·3	63·7	92·9	47·9	184·0	197·0	2·0	4·0	51·4	52·0
Sc	10·8	7·6	10·8	7·1	11·0	18·9	20·8	1·6	1·1	11·6	5·7
Co	7·6	9·3	7·6	14·0	8·5	16·7	20·6	0·4	1·0	6·0	5·0
Ni	3·0	20·7	30·3	10·6	2·4	3·2	9·5	2·0	4·7	2·8	25·9
Cu	40·3	14·5	21·4	20·4	17·3	14·3	16·6	4·1	3·6	4·2	7·8
Zn	56·0	84·1	80·6	78·5	97·7	102·0	93·3	3·9	7·2	53·1	35·0
Ga	15	22	18	20	19	20	18	13	11	19	18
Rb	97	107	119	49	124	105	98	150	134	103	28
Nb	6·9	8·7	9·7	3·6	7·4	6·0	5·1	1·5	2·8	15·1	5·2
Ba	341	341	405	304	609	197	519	757	310	184	277
Ta	0·52	0·46	0·59	0·20	0·53	0·33	0·40	0·23	0·27	0·99	0·24
Pb	16·6	14·4	9·5	10·4	14·4	5·9	7·1	32·2	44·8	15·8	8·1
Th	8·44	24·70	8·84	2·38	3·31	1·65	3·22	4·30	3·29	10·90	12·40
U	1·36	1·82	0·71	0·14	1·40	0·44	1·16	1·02	3·19	1·28	0·56
Cr	5·3	36·1	55·5	11·4	2·0	2·7	10·0	3·3	12·8	6·6	44·5
Y	21	12	32	7	33	37	22	14	24	44	17
Sr	225	398	308	470	561	602	483	205	111	271	602
Sn	1·29	2·78	3·43	0·93	4·99	3·09	3·56	0·59	2·42	2·26	0·90
Rare earth elements (ppm)											
La	25·0	75·1	37·7	15·7	28·2	13·6	13·4	8·33	8·90	36·1	52·0
Ce	43·4	133·0	74·7	30·5	61·4	31·7	29·7	17·2	16·5	76·9	99·7
Pr	5·01	13·80	8·80	3·73	8·06	4·80	4·08	1·87	2·01	7·88	10·10
Nd	17·5	43·9	32·7	14·2	34·2	23·0	18·7	6·7	7·0	27·2	35·1
Sm	3·34	6·57	6·62	2·65	7·81	6·61	4·58	1·50	1·76	5·37	4·71
Eu	0·76	1·29	1·24	1·07	2·01	1·91	1·64	0·71	1·01	1·01	1·84
Gd	3·28	4·27	6·22	2·33	6·68	6·41	4·42	1·37	1·90	6·47	3·35
Tb	0·61	0·54	1·01	0·33	0·97	0·99	0·62	0·27	0·41	1·21	0·46
Dy	3·16	2·73	6·25	1·62	5·80	6·16	4·00	2·02	3·36	8·27	2·80
Ho	0·71	0·52	1·29	0·29	1·16	1·20	0·83	0·56	0·74	1·73	0·65
Er	1·81	1·50	3·80	0·73	3·64	3·66	2·45	2·17	2·61	4·49	2·31
Tm	0·30	0·19	0·52	0·09	0·49	0·52	0·33	0·39	0·39	0·54	0·35
Yb	1·92	1·27	3·30	0·53	3·24	3·21	2·19	3·40	2·97	3·14	2·52
Lu	0·27	0·20	0·46	0·09	0·49	0·48	0·35	0·60	0·44	0·46	0·44

Table 9: The whole-rock chemical compositions of the metasedimentary rocks from the eastern Gangdese arc

Rock:	Schist					Gneiss
Sample:	T8-20-3	T9-31-9	T9-61-4	T8-44-1	T9-61-3	T8-44-7
Major elements (wt %)						
SiO_2	79·90	73·79	64·10	68·96	61·90	79·04
TiO_2	0·01	0·44	0·84	0·60	0·90	0·53
Al_2O_3	12·46	12·64	16·04	13·70	16·24	9·61
Fe_2O_3	0·44	0·13	1·12	0·98	1·26	0·42
FeO	0·24	2·07	6·90	5·01	6·41	2·85
MnO	0·01	0·23	0·14	0·15	0·18	0·07
MgO	0·22	1·22	3·06	2·89	3·52	1·27
CaO	1·05	7·89	2·10	1·81	2·73	1·81
Na_2O	2·47	0·20	1·66	1·57	2·34	1·61
K_2O	1·47	0·08	2·12	2·63	2·22	1·99
P_2O_5	0·02	0·13	0·08	0·07	0·13	0·13
H_2O	1·14	0·60	1·59	0·47	1·77	0·43
LOI	1·30	0·57	1·29	1·40	1·53	0·89
Total	99·59	99·39	99·45	99·77	99·36	100·22
Trace elements (ppm)						
Hf	0·53	4·71	4·66	10·3	4·19	11·64
Zr	13	150	167	200	154	357
V	25	33	183	91	202	54
Sc	1·3	6·4	26	18	24	11
Co	0·9	6·4	14·2	17·3	19·2	8·9
Ni	2·3	17	21	35	42	13
Cu	4·0	21	34	13	30	8
Zn	2·5	45	101	106	110	60
Ga	11	16	19	18	21	12
Rb	33	3·4	84	107	92	65
Nb	0·5	12	12	17	10	7·1
Ba	697	140	336	653	314	432
Ta	0·03	1·19	0·66	0·86	0·52	0·37
Pb	7·2	8·6	13·3	19·2	14·3	16·7
Th	0·46	22	14	28	17	16
U	0·04	5·19	1·01	1·62	1·20	1·51
Cr	8·0	40	130	72	144	29
Y	0·83	15	39	44	33	35
Sr	223	379	151	136	241	76
Sn	1·16	3·95	0·80	0·27	0·81	0·43
Rare earth elements (ppm)						
La	0·30	44·5	35·2	56·2	42·2	44·8
Ce	0·56	81·7	68·5	110·2	82·4	82·2
Pr	0·08	9·15	7·90	13·15	9·38	9·75
Nd	0·40	31·2	29·2	47·8	34·6	34·9
Sm	0·10	5·54	5·71	8·87	6·65	6·67
Eu	0·04	1·26	1·34	1·27	1·38	1·25
Gd	0·07	4·24	5·49	6·82	5·95	5·38
Tb	0·02	0·60	1·06	1·20	1·00	0·92
Dy	0·10	3·27	7·48	6·83	6·39	5·16
Ho	0·02	0·61	1·63	1·55	1·31	1·20
Er	0·07	1·81	4·90	4·58	3·96	3·59
Tm	0·01	0·24	0·70	0·80	0·54	0·64
Yb	0·11	1·69	4·54	5·07	3·39	3·99
Lu	0·02	0·26	0·71	0·75	0·53	0·55

similar to those of detrital zircons in the Nyingchi paragneiss. These correlations suggest that the S-type granites formed by crustal anatexis of the Nyingchi paragneiss at depth. In addition, Wang *et al.* (2008) reported a granitic vein formed by anatexis of amphibolite in the Nyingchi complex at ~65 Ma. Palin *et al.* (2013) concluded that pelitic migmatites from the studied area underwent Paleocene to Eocene granulite-facies metamorphism and partial melting. Our study further shows that Mesozoic sedimentary rocks from the southern Lhasa terrane have been buried to lower crustal depths and experienced granulite-facies metamorphism and partial melting during the Paleocene. These features suggest that the migmatitic metasedimentary rocks of the Nyingchi complex could be the magma source for the Paleocene S-type granites of the Gangdese arc.

Paleocene metamorphism of the Gangdese arc

Recent studies indicate that the Gangdese batholiths have experienced multiphase metamorphism from Late Mesozoic to Early Cenozoic times (Zhang *et al.*, 2009, 2010*a*, 2012*a*; Dong *et al.*, 2010*b*; Guo *et al.*, 2011, 2012). Our study further shows that the Paleocene Gangdese plutons underwent nearly syn-intrusion granulite-facies metamorphism, indicating that these plutons were emplaced at lower crustal depths within the Gangdese arc. In addition, the Paleocene granodiorites contain igneous epidote, which is an index mineral of deep crustal magmatic rocks (Zen & Hammarstrom, 1984; Brown & Walker, 1993; Schmidt & Poli, 2004). Wen *et al.* (2008*a*) and Zhang, H. F., *et al.* (2010) also concluded that the presence of primary epidote in the Gangdese granitoids from the Nyingchi area is indicative of intrusion at depths within the middle to lower crust.

As described above, recent studies and the present work have demonstrated that the Nyingchi complex underwent Mesozoic–Cenozoic amphibolite- to granulite-facies metamorphism and related anatexis. Moreover, our geochronological data reveal that Paleocene plutonism, granulite-facies metamorphism and crustal anatexis are almost contemporaneous in the Gangdese arc, indicating an accretionary orogenic episode characterized by high heat flow, granulite-facies metamorphism and partial melting, which are diagnostic features of active continental margins, representing the sites of mantle-derived magma accretion and continental crust generation (e.g. Collins, 2002*a*, 2002*b*; Hyndman *et al.*, 2005; Currie & Hyndman, 2006; Klepeis *et al.*, 2007; Scott *et al.*, 2009). Such magma accretion resulting in crustal thickening and growth, and associated granulite-facies metamorphism may be one of the most important processes in subduction-related magmatic arcs (Gibson *et al.*, 1988; Brown & Walker, 1993; Brown, 1996; Yoshino *et al.*, 1998; Clarke *et al.*, 2000;

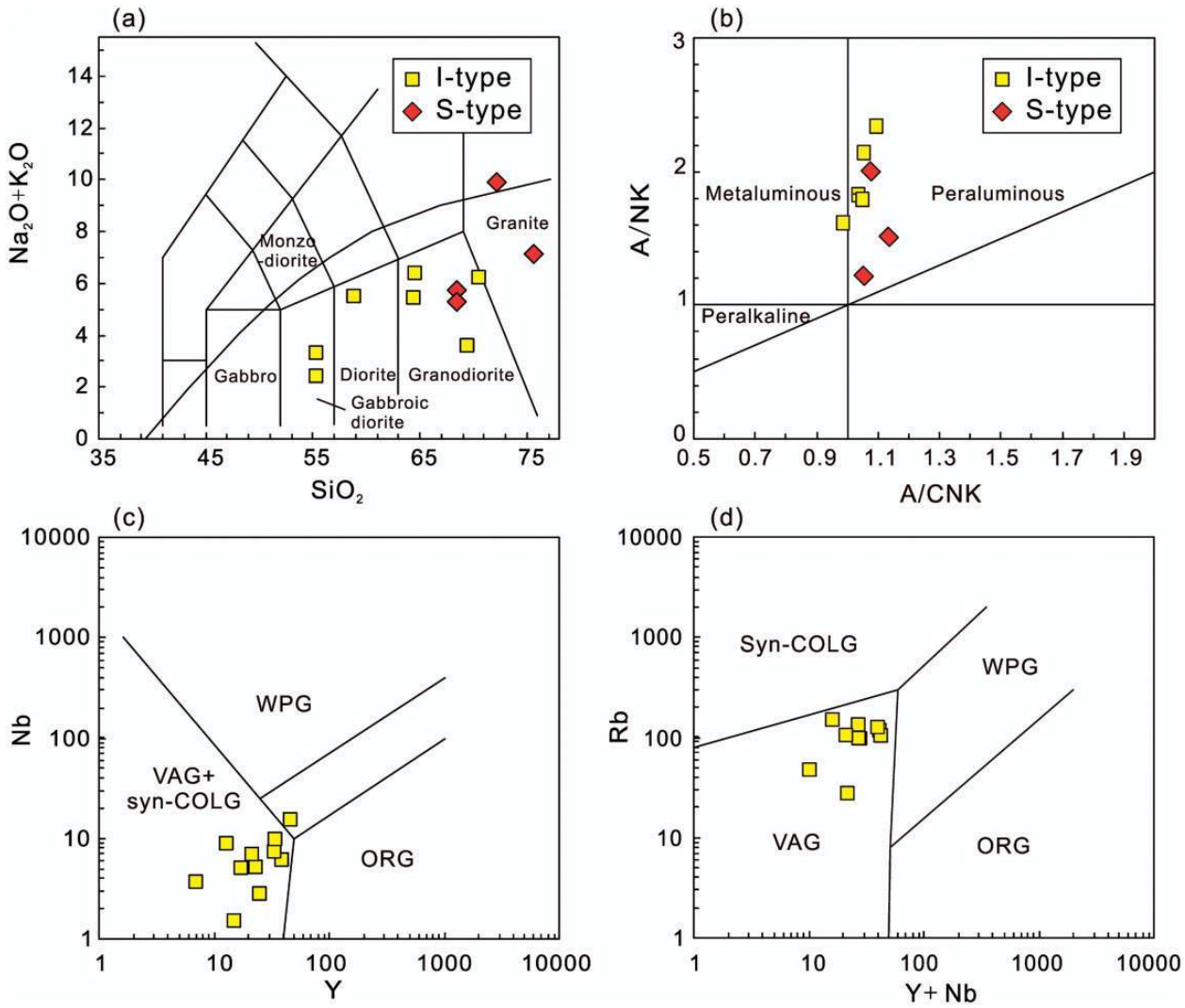

Fig. 7. Compositional variations within the analyzed Gangdese granitoids. (a) SiO_2 vs $Na_2O + K_2O$ classification diagram (after Middlemost, 1994); (b) A/CNK vs A/NK classification diagram (after Shand, 1951); (c) Y vs Nb discrimination diagram (after Pearce *et al.*, 1984); (d) Rb vs Y + Nb discrimination diagram (after Pearce *et al.*, 1984). ORG, ocean ridge granite; Syn-COLG, syn-collision granite; VAG, volcanic arc granite; WPG, within-plate granite.

Müntener *et al.*, 2000; Collins, 2002*a*, 2003; Hollis *et al.*, 2003, 2004; Scott *et al.*, 2009; Stowell *et al.*, 2010).

As mentioned above, our phase equilibrium modeling shows that the pelitic schists from the Nyingchi complex underwent a significant near-isobaric cooling in the granulite-facies field, with a temperature decrease of *c.* 100°C at nearly constant pressure of *c.* 10 kbar (Figs 9 and 10). During this cooling process, sillimanite-bearing schist and garnet–biotite schist are replaced by kyanite-bearing schist (sample T9-61-4), and garnet–two-mica schist (sample T9-6-3), respectively (Figs 4, 9 and 10). Harley (1989) concluded that granulites with isobaric cooling *P–T* paths may form in and beneath areas of voluminous magmatic accretion, and that kyanite could develop as a late phase in isobarically cooled granulites at pressures greater than 6 kbar. Many studies have indicated that the formation of granulites with an anticlockwise *P–T* path involving near-isobaric cooling following the peak-metamorphism were most probably related to the intrusion and underplating of mantle-derived magmas (Bohlen, 1987, 1991; Ellis, 1987; Müntener *et al.*, 2000; Zhao & Zhai, 2013, and references therein). In the eastern Himalayan syntaxis, the Kohistan arc complex represents a Cretaceous intra-oceanic arc formed during the northward subduction of Neo-Tethyan oceanic lithosphere beneath the Karakoram (e.g. Burg *et al.*, 1998; Anczkiewicz & Vance, 2000; Schaltegger *et al.*, 2002; Dhuime *et al.*, 2007; Jagoutz *et al.*, 2009; Bosch *et al.*, 2011).

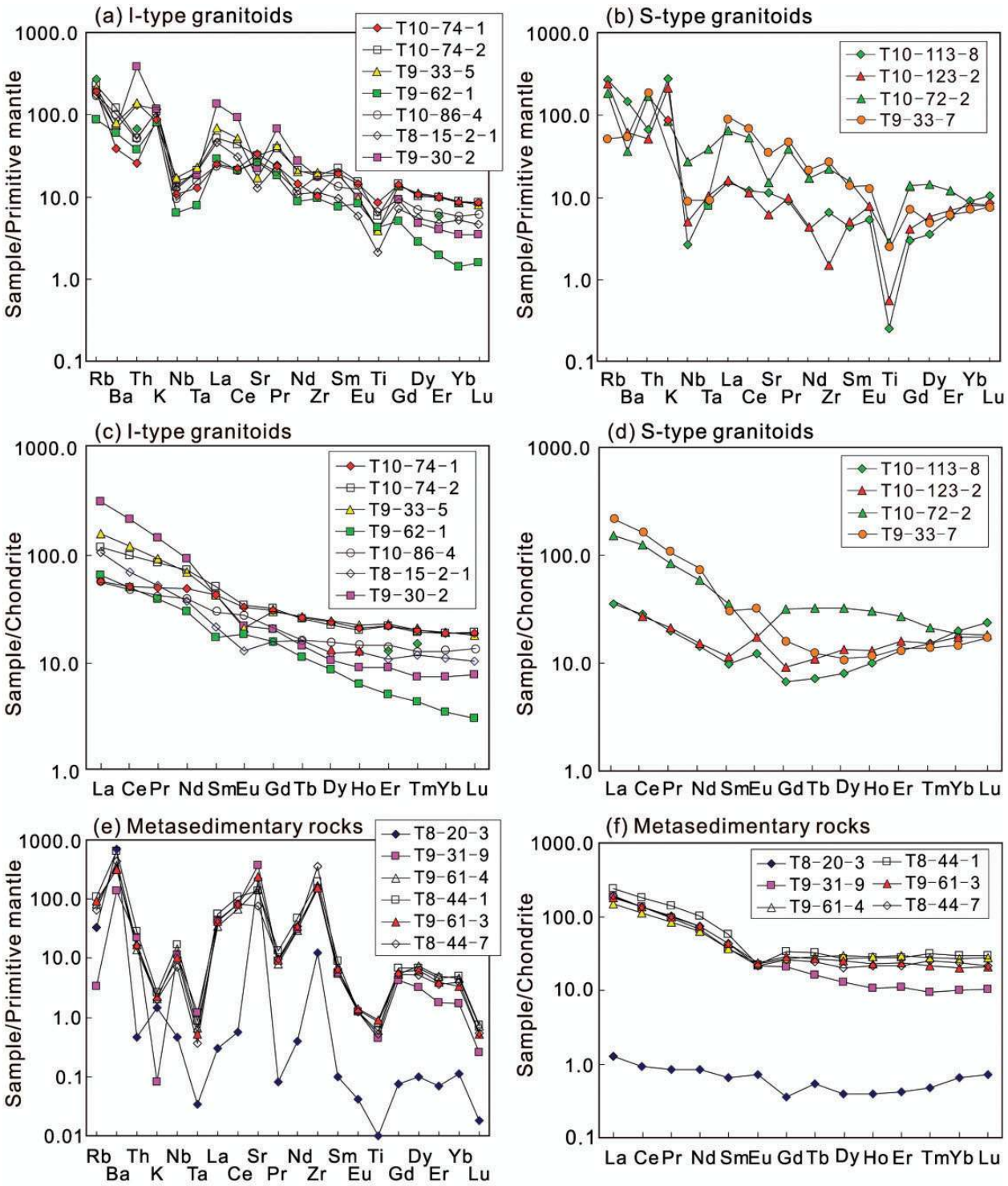

Fig. 8. Primitive-mantle normalized trace element and chondrite-normalized REE patterns of the studied rocks. (a, c) Paleocene I-type granitoids; (b, d) S-type granites; (e, f) metasedimentary rocks.

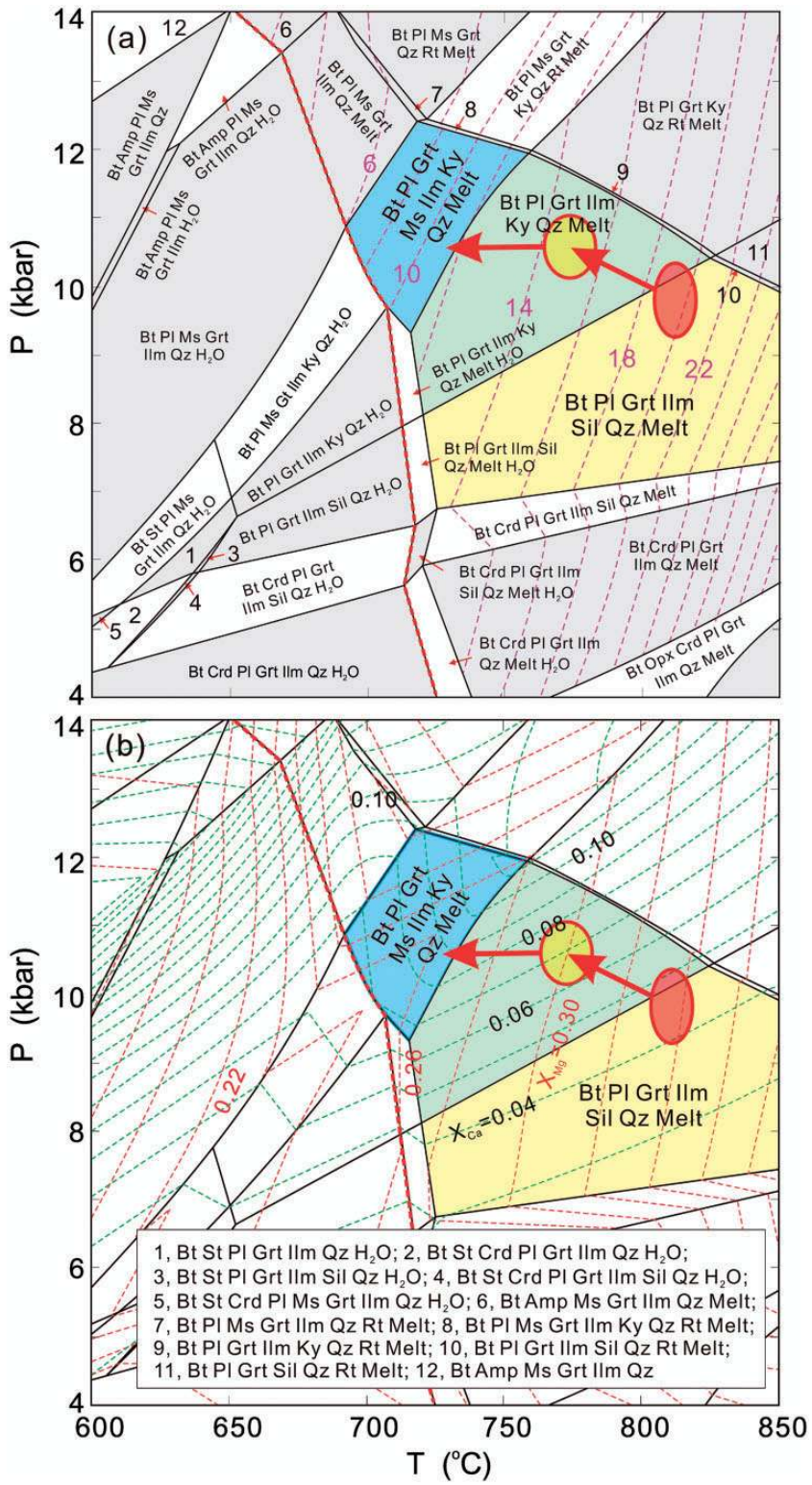

Fig. 9. (a) P–T pseudosection constructed with the bulk composition of sample T9-6l-4. The pink, thin dashed isopleths correspond to melt modal proportions (in 2 vol. % interval); the thick red dashed line is the H_2O saturated solidus. (b) Garnet composition isopleths. The red and green dashed lines represent isopleths of X_{Mg} [Fe/(Fe + Mg)] and X_{Ca} [Ca/(Fe + Mg + Ca + Mn)] for garnet, respectively. The mineral assemblages marked by numbers in (a) are listed in the lower part of (b). The semitransparent red and yellow circles refer to the P–T fields calculated from the composition isopleths of garnet cores and inner rims, respectively. The red lines with arrows represent the retrograde P–T path.

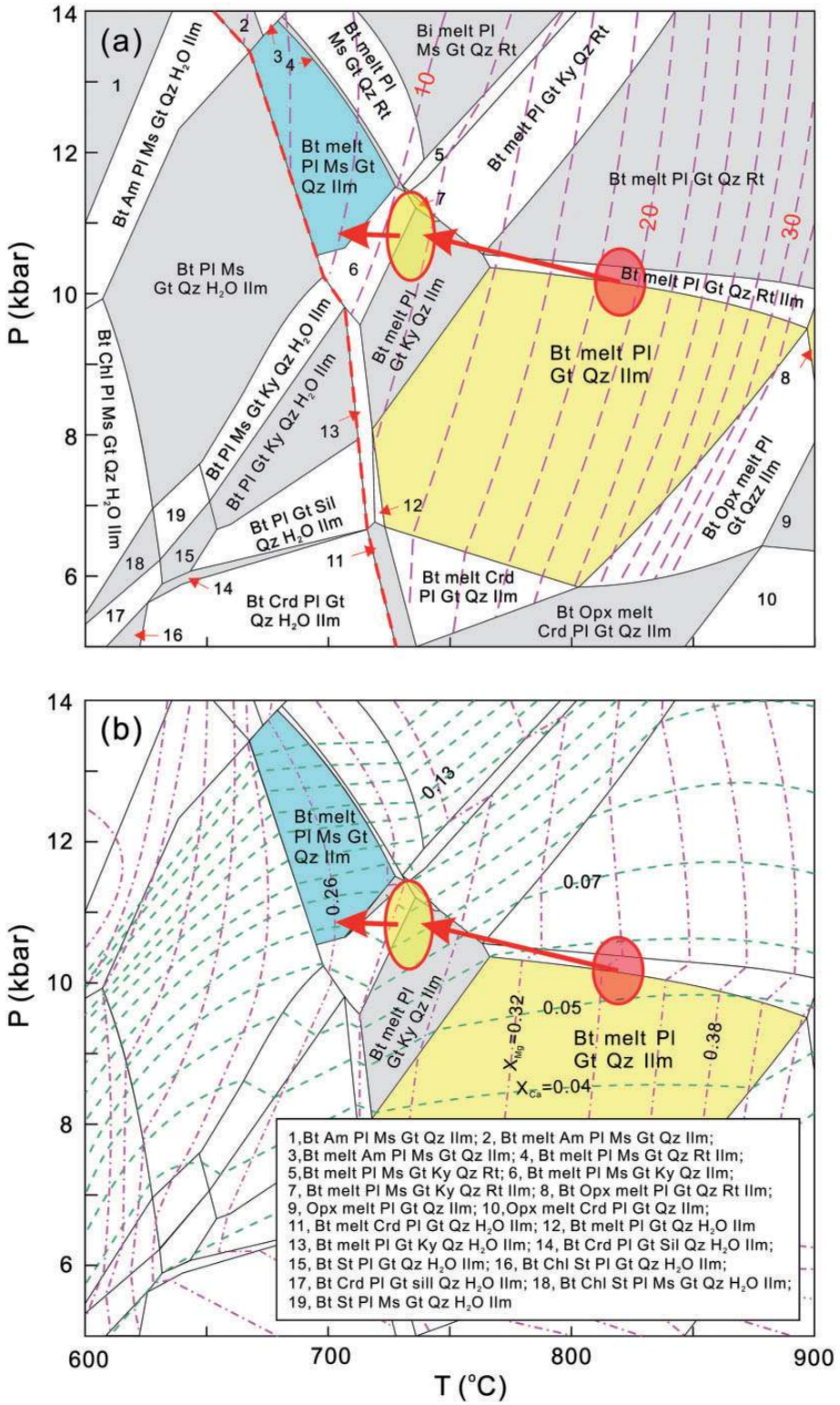

Fig. 10. (a) P–T pseudosection constructed with the bulk composition of sample T9-61-3. The pink dashed isopleths correspond to melt modal proportions (in 2 vol. % interval); the thick red dashed line is the H_2O saturated solidus. (b) Garnet composition isopleths. The pink and green dashed lines represent isopleths of X_{Mg} and X_{Ca} for garnet, respectively. The mineral assemblages marked by numbers in (a) are listed in the lower part of (b). The semitransparent red and yellow circles refer to the P–T fields calculated from the composition isopleths of garnet cores and inner rims, respectively. The red lines with arrows represent the retrograde P–T path.

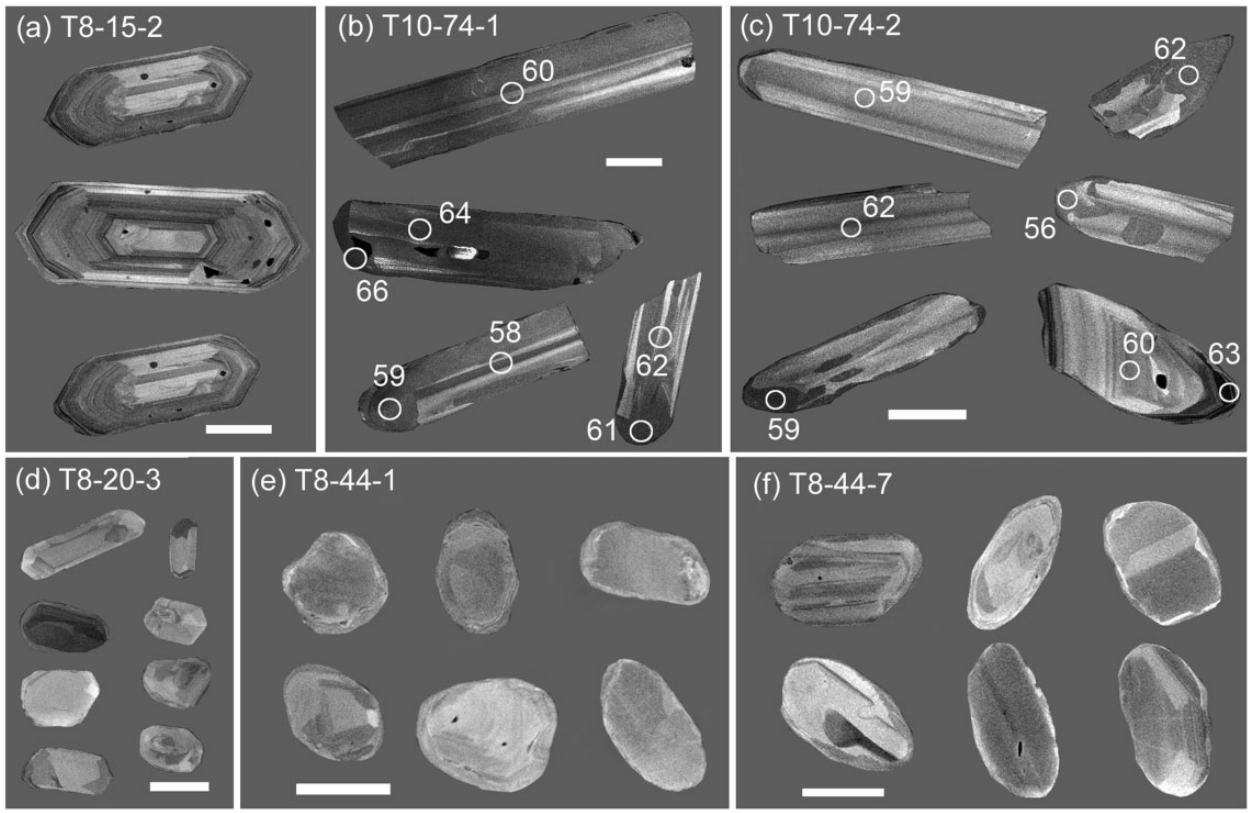

Fig. 11. CL images of zircons from granitoid (a), meta-granitoids (b, c), schist (d) the metasedimentary rocks (e, f), showing the analytical spots (circles) and related ages (in Ma) of the two meta-granitoids. The scale bars represent 100 μm.

The lower-crustal rocks of the Kohistan arc are composed of high-pressure granulites (Yamamoto, 1993; Yamamoto & Nakamura, 1996, 2000; Yamamoto & Yoshino, 1998; Yoshino *et al.*, 1998; Schaltegger *et al.*, 2002; Garrido *et al.*, 2006, 2007; Jagoutz *et al.*, 2006; Padron-Navarta *et al.*, 2008; Bosch *et al.*, 2011). Although many studies have proposed a crustal thickening model resulted from magmatic accretion and loading within the middle crust for the lower crustal evolution of the Kohistan arc (e.g. Khan *et al.*, 1998; Yoshino *et al.*, 1998; Yoshino & Okudaira, 2004; Heuberger *et al.*, 2007; Dhuime *et al.*, 2009), Ringuette *et al.* (1999) suggested an alternative model of magmatic crystallization, isobaric cooling, and decompression for the origin of the Kohistan arc granulites. This model is consistent with the intrusive bodies occurring at variable levels within the Kohistan arc complex (Jagoutz, 2010), and with experimental studies on igneous garnet and amphibole fractionation from andesitic liquids at conditions comparable with those for the roots of island arcs (Alonso-Perez *et al.*, 2009). Moreover, several studies have proposed that advective heating caused by magmatic accretion could have triggered granulite formation in the middle and lower crust of magmatic arcs (Bohlen, 1987, 1991; Ellis, 1987; Robb *et al.*, 1999; Müntener *et al.*, 2000; Stowell *et al.*, 2010). Our study shows that the Nyingchi complex did not experience the isothermal (or heating) increasing pressure process, which would be related to crustal thickening owing to magma loading. In contrast, the Nyingchi complex records only a near-isobaric cooling process, typical of magma accretion. Thus, we infer that the Paleogene HT and HP metamorphism and subsequent near-isobaric cooling of the Nyingchi complex are essentially the result of magmatic accretion, and heating and late heat relaxation in the lower crust of the Gangdese arc. This conclusion is consistent with the inference that the Paleocene is the most prominent magmatic episode within the Gangdese arc, as mentioned above.

Recently, Palin *et al.* (2013) carried out *in situ* U–Pb dating of monazite in pelitic schists from the Nyingchi complex. Their results show that the metamorphism of the sillimanite-grade and kyanite-grade schists and nearly coeval partial melting occurred at *c.* 71–50 Ma and *c.* 57–44 Ma, respectively. They considered that these tectonothermal events were related to regional heat advection caused by coeval and prolonged emplacement of Gangdese batholith units. These data provide an important time constraint on the sillimanite-grade metamorphism of the pelitic schist preceding the kyanite-grade

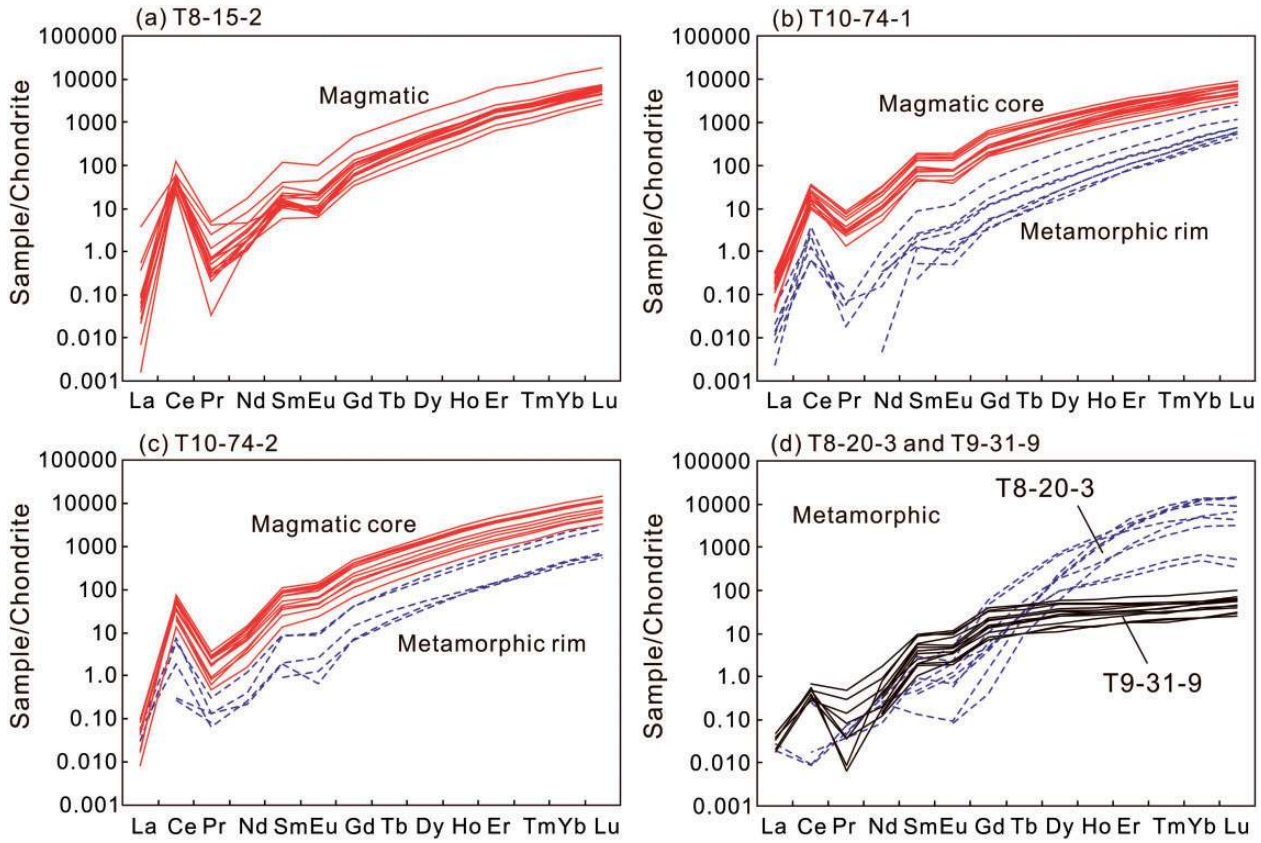

Fig. 12. Chondrite-normalized REE patterns of zircons from granitoid (a), meta-granitoids (b, c) and schists (d).

metamorphism in the Nyingchi complex, as revealed independently by the petrological and thermobarometric evidence from the present study. This result also indicates that the Early Paleogene anatexis of the Gangdese lower crust may have been sustained for up to 10 Myr, which is broadly consistent with the duration of magmatism and metamorphism (from 66 to 52 Ma) revealed by our study.

Tectonic model

As mentioned above, the Gangdese arc within the southern Lhasa terrane was an Andean-type active continental margin that resulted from the northward subduction of Neo-Tethyan oceanic lithosphere prior to India–Asia collision. After a period of continuous subduction *c.* 100–85 Ma, which resulted in the formation of extensive Cretaceous intrusions and associated volcanic rocks (Chu *et al.*, 2006; Wen *et al.*, 2008*a*; Ji *et al.*, 2009; Lee *et al.*, 2009), a magmatic gap or quiescent period occurred between 80 and 70 Ma, which led some investigators to suggest a period of low-angle or flat subduction of the Neo-Tethyan oceanic slab (Coulon *et al.*, 1986; Chung *et al.*, 2005; Wen *et al.*, 2008*a*, 2008*b*; Lee *et al.*, 2009). The intensification of Paleogene magmatism has been interpreted as the consequence of roll-back or steepening of the subducted Neo-Tethyan oceanic slab (Coulon *et al.*, 1986; Ding *et al.*, 2003; Chung *et al.*, 2005; Kapp *et al.*, 2005*b*, 2007; Wen *et al.*, 2008*a*; Lee *et al.*, 2009). Slab roll-back would result in strong crustal shortening (>40%) (Guo *et al.*, 2012), and enhanced asthenospheric corner flow changing the thermal structure of the mantle wedge (Chung *et al.*, 2003). Roll-back would also allow an influx of mantle-derived magma above the retreating slab, providing a source of heat for metamorphism, melting and magmatism in the southern Lhasa terrane (Guo *et al.*, 2012).

Our study further reveals that the Paleocene accretionary orogenic episode of the Gangdese arc is characterized by extensive plutonism and coeval regional granulite-facies metamorphism and crustal anatexis. Based on our new data and previously published data, we infer that the roll-back of the flat subducted Neo-Tethyan slab during the Late Mesozoic resulted in a contractional orogenic regime, increase of asthenospheric corner flow and injection of voluminous mantle-derived magmas (Fig. 17). Hence, shortening of the southern Lhasa terrane, deep burial of sedimentary rocks, and large-scale heating of the lower crust resulted in the extensive granulite-facies metamorphism and I-type and S-type granitoid magmatism of the lower crust of the Gangdese arc (Fig. 17).

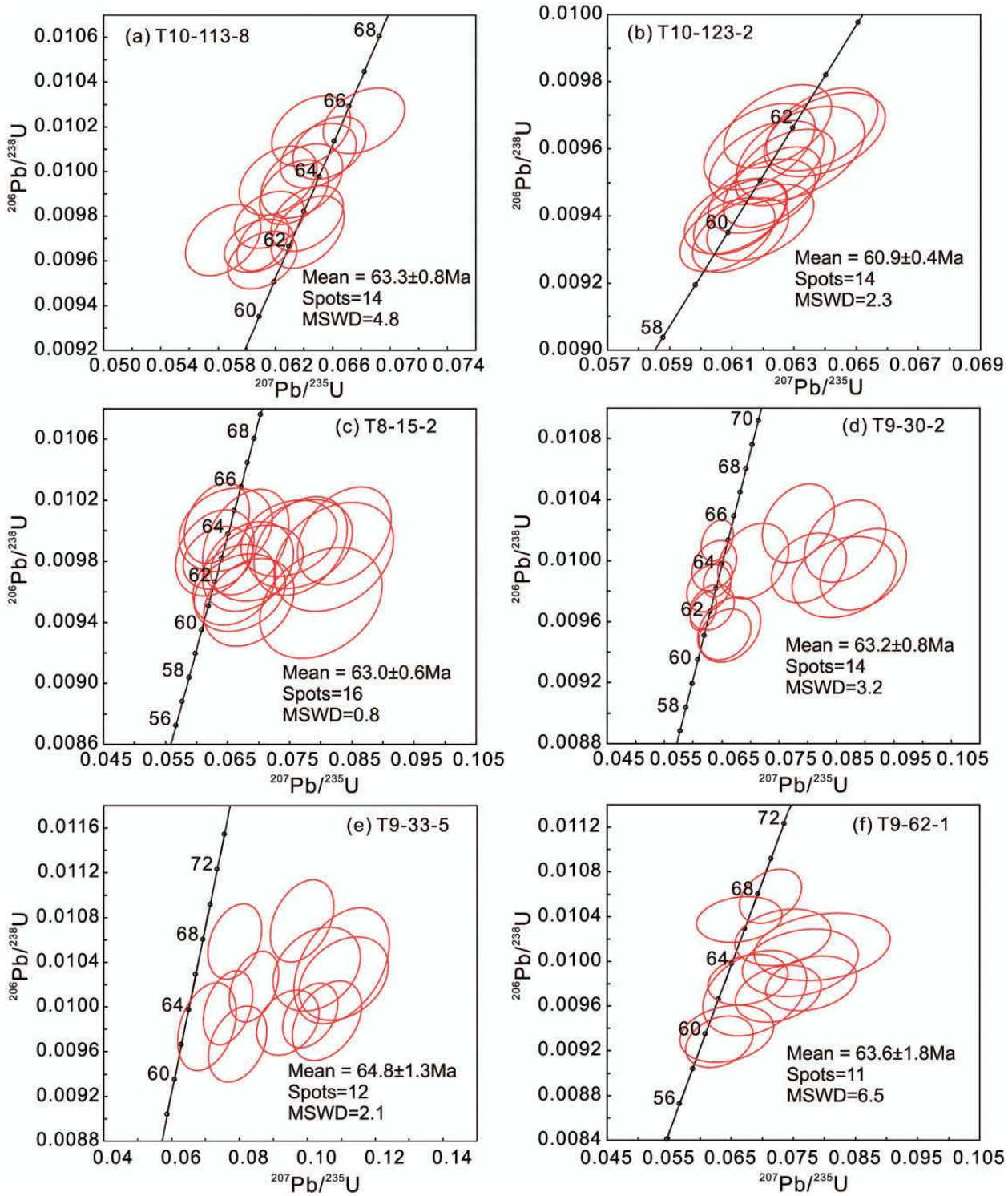

Fig. 13. Zircon U–Pb concordia diagrams for the granitoids.

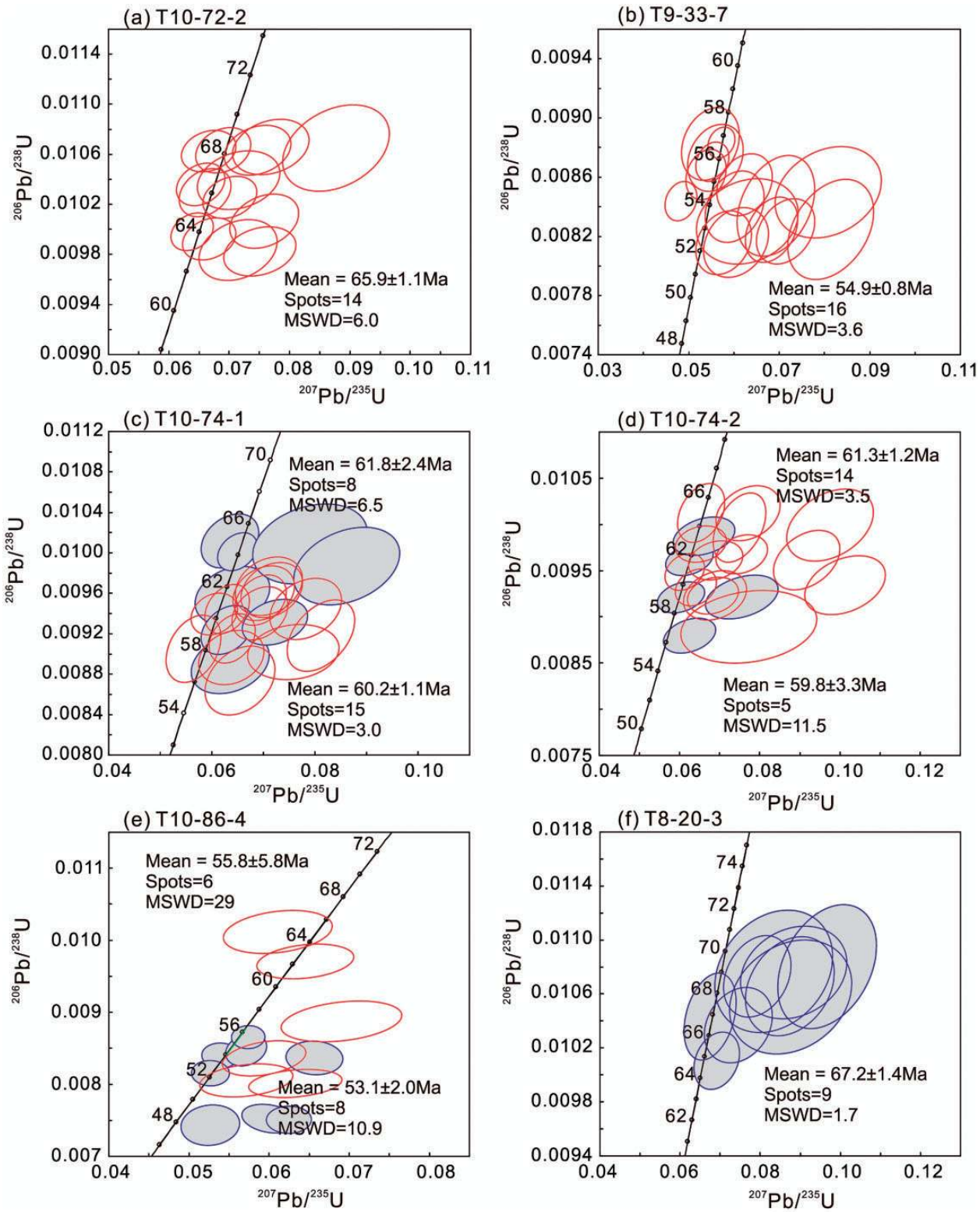

Fig. 14. Zircon U–Pb concordia diagrams for granitoids (a, b), meta-granitoids (c–e) and schist (f). Open and grey-filled ellipses represent magmatic and metamorphic zircons, respectively.

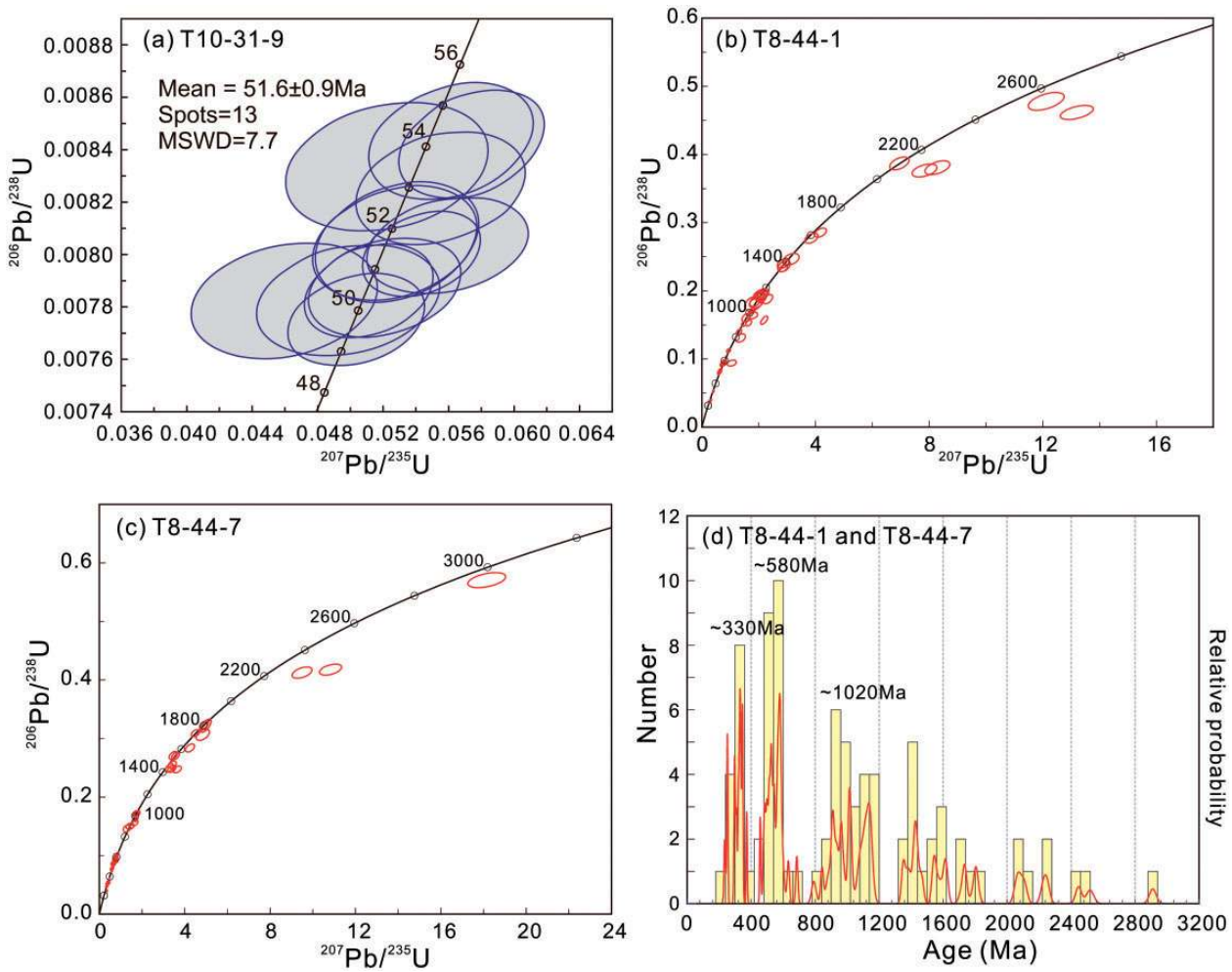

Fig. 15. Zircon U–Pb concordia diagrams (a–c) and a relative probability diagram (d) for inherited zircons from metasedimentary rocks. Grey-filled and open ellipses represent metamorphic and magmatic zircons, respectively.

Further investigations are required to test the proposed model for magma accretion and lower crustal heating and to exclude alternative tectonic models, such as the magma-loading (Brown & Walker, 1993; Brown, 1996; Yoshino & Okudaira, 2004; Heuberger *et al.*, 2007; Dhuime *et al.*, 2009) and the subduction erosion models (Kay & Mpodozis, 2002; Stern, 2011, and references therein). The petrological, geochemical and geochronological data provided by our study reveal a long-lived magmatic and metamorphic process, and hence provide new insights into deep crustal processes within the Gangdese arc.

CONCLUSIONS

The Nyingchi complex in the southeastern Lhasa terrane consists of plutonic rocks, their metamorphosed equivalents (orthogneisses), and metasedimentary rocks. These rocks record Paleocene magmatism and metamorphism during the northward subduction of Neo-Tethyan ocean lithosphere beneath the Lhasa terrane. These deep-seated intrusions and HT and HP granulites represent the original lower crust of the Gangdese magmatic arc.

We propose a model that envisages that the roll-back of a flat-subducted Neo-Tethyan slab resulted in contractional orogeny and accretion of voluminous deep-seated intrusions. These in turn caused extensive crustal heating of the Gangdese arc to generate granulite-facies metamorphism and partial melting of the deep-seated plutons and deeply buried supracrustal rocks. Thus, the Paleocene Gangdese arc provides a typical example with which to link the processes of formation of granulites, silicic magmatism, and crustal growth during an accretionary orogeny.

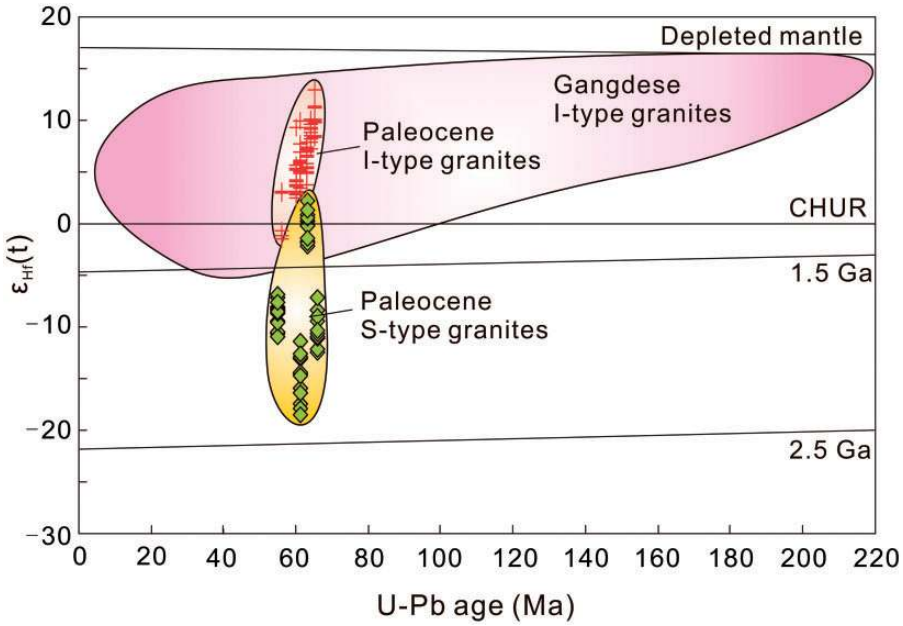

Fig. 16. Plot of $\varepsilon_{Hf}(t)$ vs U–Pb age for zircons from the granitoids. The field of Gangdese I-type granites is from Ji *et al.* (2009), and the fields of Paleocene I- and S-type granites are from the present study.

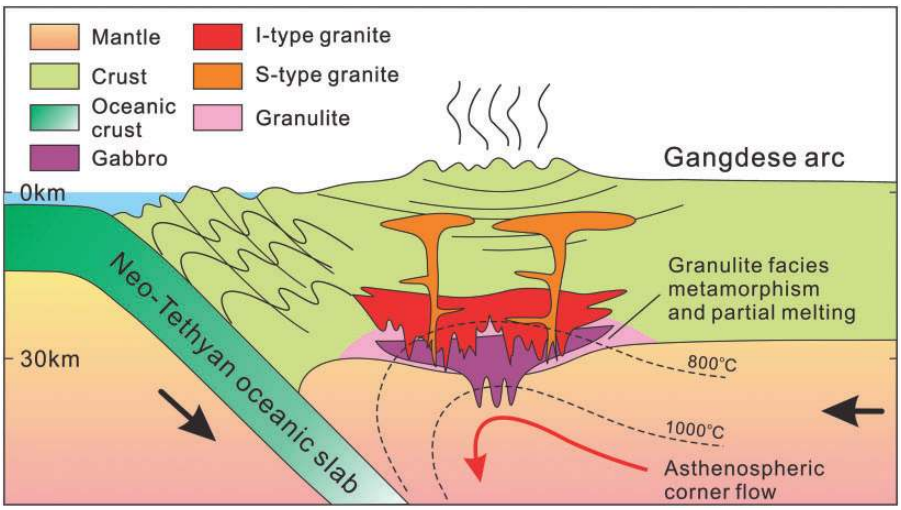

Fig. 17. Paleocene tectonic model for the southeastern Gangdese arc. Steep subduction of the Neo-Tethyan oceanic lithosphere resulted in the contraction of the Gangdese crust and the deep burial of sedimentary rocks. The increase in asthenosphere corner flow and intrusion of mantle-derived magma into the crust resulted in extensive heating, which caused granulite-facies metamorphism and I- and S-type magmatism in the lower crust of the Gangdese arc. The black dashed lines are the hypothetical isotherms for the lower crust and upper mantle of the Gangdese arc.

ACKNOWLEDGEMENTS

Zeming Zhang thanks Professors Zhiqin Xu, Zhenmin Jin, Dicheng Zhu, Lailin Zheng, Linsheng Zheng, Xunxiang Qi, Yongsheng Liu and Zhaochu Hu and Keqing Zong for their valuable guidance and discussions during our investigation.

FUNDING

This research is co-supported by the National Natural Science Foundation of China (41230205, 40921001 and 40921001) and the China Geological Survey (1212010918012).

SUPPLEMENTARY DATA

Supplementary data for this paper are available at *Journal of Petrology* online.

REFERENCES

Aitchison, J. C., Xia, X., Baxter, A. T. & Ali, J. R. (2011). Detrital zircon U–Pb ages along the Yarlung–Tsangpo suture zone, Tibet: Implications for oblique convergence and collision between India and Asia. *Gondwana Research* **20**, 691–709.

Allègre, C. J., Courtillot, V., Tapponnier, P. *et al*. (1984). Structure and evolution of the Himalaya–Tibet orogenic belt. *Nature* **307**, 17–22.

Alonso-Perez, R., Müntener, O. & Ulmer, P. (2009). Igneous garnet and amphibole fractionation in the roots of island arcs: Experimental constraints on andesitic liquids. *Contributions to Mineralogy and Petrology* **157**, 541–558.

Anczkiewicz, R. & Vance, D. (2000). Isotopic constraints on the evolution of metamorphic conditions in the Jijal–Patan Complex and Kamila Belt of the Kohistan Arc, Pakistan Himalaya. In: Khan, M. A., Treloar, P. J., Searle, M. P. & Jan, M. Q. (eds) *Tectonics of the Nanga Parbat Syntaxis and the Western Himalaya. Geological Society, London, Special Publications* **170**, 321–331.

Barbarin, B. (1998). A review of the relationships between granitoid types, their origins and their geodynamic environments. *Lithos* **46**, 605–626.

Barth, M., McDonough, W. & Rudnick, R. L. (2000). Tracking the budget of Nb and Ta in the continental crust. *Chemical Geology* **165**, 197–213.

Bignold, S. M. & Treloar, P. J. (2003). Northward subduction of the Indian plate beneath the Kohistan island arc, Pakistan Himalaya: New evidence from isotopic data. *Journal of the Geological Society, London* **160**, 377–384.

Bohlen, S. R. (1987). Pressure–temperature–time paths and a tectonic model for the evolution of granulites. *Journal of Geology* **95**, 617–632.

Bohlen, S. R. (1991). On the formation of granulites. *Journal of Metamorphic Geology* **9**, 223–229.

Bosch, D., Garrido, C. J., Bruguier, O., Dhuime, B., Bodinier, J. L., Padron-Navarta, J. A. & Galland, B. (2011). Building an island-arc crustal section: Time constraints from a LA-ICP-MS zircon study. *Earth and Planetary Science Letters* **309**, 268–279.

Brown, E. H. (1996). High-pressure metamorphism caused by magma loading in Fiordland, New Zealand. *Journal of Metamorphic Geology* **14**, 441–452.

Brown, E. H. & Walker, N. W. (1993). A magma loading model for Barrovian metamorphism in the southeast Coast Plutonic Complex, British Columbia and Washington. *Geological Society of America Bulletin* **105**, 479–500.

Burenjargal, U., Okamoto, A., Meguro, Y. & Tsuchiya, N. (2012). An exhumation pressure–temperature path and fluid activities during metamorphism in the Tseel terrane, SW Mongolia: Constraints from aluminosilicate-bearing quartz veins and garnet zonings in metapelites. *Journal of Asian Earth Sciences* **54–55**, 214–229.

Burg, J. P. & Chen, G. M. (1984). Tectonics and structural formation of southern Tibet, China. *Nature* **311**, 219–223.

Burg, J., Davy, P., Nievergelt, P., Oberli, F., Seward, D., Diao, Z. & Meier, M. (1997). Exhumation during crustal folding in the Namche–Barwa syntaxis. *Terra Nova* **9**, 53–56.

Burg, J.-P., Bodinier, J.-L., Chaudhry, S., Hussain, S. & Dawood, H. (1998). Infra-arc mantle–crust transition and intra-arc mantle diapirs in the Kohistan Complex (Pakistani Himalaya): petro-structural evidence. *Terra Nova* **10**, 74–80.

Cawthorn, R. G. & O'Hara, M. J. (1976). Amphibole fractionation in calc-alkaline magma genesis. *American Journal of Science* **276**, 309–329.

Chatterjee, S., Goswami, A. & Scotese, R. (2013). The longest voyage: Tectonic, magmatic, and paleoclimatic evolution of the Indian plate during its northward flight from Gondwana to Asia. *Gondwana Research* **23**, 238–267.

Chiu, H. Y., Chung, S. L., Wu, F. Y., Liu, D. Y., Liang, Y. H., Lin, Y. J., Iizuka, Y., Xie, L. W., Wang, Y. B. & Chu, M. F. (2009). Zircon U–Pb and Hf isotope constraints from eastern Transhimalayan batholiths on the precollisional magmatic and tectonic evolution in southern Tibet. *Tectonophysics* **477**, 3–19.

Chu, M. F., Chung, S. L., Song, B., Liu, D. Y., O'Reilly, S. Y., Pearson, N. J., Ji, J. Q. & Wen, D. J. (2006). Zircon U–Pb and Hf isotope constraints on the Mesozoic tectonics and crustal evolution of Southern Tibet. *Geology* **34**, 745–748.

Chung, S. L., Liu, D. Y., Ji, J. Q., Chu, M. F., Lee, H. Y., Wen, D. J., Lo, C. H., Lee, T. Y., Qian, Q. & Zhang, Q. (2003). Adakites from continental collision zones: melting of thickened lower crust beneath southern Tibet. *Geology* **31**, 1021–1024.

Chung, S. L., Chu, M. F., Zhang, Y. Q., Xie, Y. W., Lo, C. H., Lee, T. Y., Lan, C. Y., Li, X. H., Zhang, Q. & Wang, Y. Z. (2005). Tibetan tectonic evolution inferred from spatial and temporal variations in post-collisional magmatism. *Earth-Science Reviews* **68**, 173–196.

Chung, S. L., Chu, M. F., Ji, J. Q., O'Reilly, S. Y., Pearson, N. J., Liu, D. Y., Lee, T. Y. & Lo, C. H. (2009). The nature and timing of crustal thickening in Southern Tibet: Geochemical and zircon Hf isotopic constraints from postcollisional adakites. *Tectonophysics* **477**, 36–48.

Clarke, G. L., Klepeis, K. A. & Daczko, N. R. (2000). Cretaceous high-*P* granulites at Milford Sound, New Zealand: metamorphic history and emplacement in a convergent margin setting. *Journal of Metamorphic Geology* **18**, 359–374.

Coggon, R. & Holland, T. J. B. (2002). Mixing properties of phengitic micas and revised garnet–phengite thermobarometers. *Journal of Metamorphic Geology* **20**, 683–696.

Collins, W. L. (2002*a*). Hot orogens, tectonic switching, and creation of continental crust. *Geology* **30**, 535–538.

Collins, W. L. (2002*b*). Nature of extensional accretionary orogens. *Tectonics* **21**, 1024, doi:10.1029/2000TC001272.

Collins, W. J. (2003). Hot orogens, tectonic switching, and creation of continental crust: comment and reply: reply. *Geology* **31**, e10.

Collins, W. J. & Richards, S. W. (2008). Geodynamic significance of S-type granites in circum-Pacific orogens. *Geology* **36**, 559–562.

Connolly, J. A. D. (2005). Computation of phase equilibria by linear programming: a tool for geodynamic modeling and its application to subduction zone decarbonation. *Earth and Planetary Science Letters* **236**, 524–541.

Coulon, C., Maluski, H., Bollinger, C. & Wang, S. (1986). Mesozoic and Cenozoic volcanic rocks from central and southern Tibet: ^{39}Ar–^{40}Ar dating, petrological characteristics and geodynamical significance. *Earth and Planetary Science Letters* **79**, 281–302.

Currie, C. A. & Hyndman, R. D. (2006). The thermal structure of subduction zone back arcs. *Journal of Geophysics Research* **111**, B08404, doi:10.1029/2005JB004024.

Daczko, N. R., Klepeis, K. A. & Clarke, G. L. (2002). Thermomechanical evolution of the crust during convergence and deep crustal pluton emplacement in the Western Province of Fiordland, New Zealand. *Tectonics* **21**, 4-1–4-18.

Debon, F., Le Fort, P., Sheppard, S. M. F. & Sonet, J. (1986). The four plutonic belts of the Transhimalaya–Himalaya: a chemical,

mineralogical, isotopic, and chronological synthesis along a Tibet–Nepal section. *Journal of Petrology* **27**, 219–250.

Dhuime, B., Bosch, D., Bodinier, J. L., Garrido, C. J., Bruguier, O., Hussain, S. S. & Dawood, H. (2007). Multistage evolution of the Jijal ultramafic–mafic complex (Kohistan, N Pakistan): Implications for building the roots of island arcs. *Earth and Planetary Science Letters* **261**, 179–200, doi:10.1016/j.epsl.2007.06.026.

Dhuime, B., Bosch, D., Garrido, C. J., Bodinier, J. L., Bruguier, O., Hussain, S. S. & Dawood, H. (2009). Geochemical architecture of the lower- to middle-crustal section of a paleo-island arc (Kohistan Complex, Jijal–Kamila area, northern Pakistan): implications for the evolution of an oceanic subduction zone. *Journal of Petrology* **50**, 531–569.

Diener, J. F. A., Powell, R., White, R. W. & Holland, T. J. B. (2007). A new thermodynamic model for clino- and orthoamphiboles in the system Na_2O–CaO–FeO–MgO–Al_2O_3–SiO_2–H_2O–O. *Journal of Metamorphic Geology* **25**, 631–656.

Ding, L., Kapp, P., Zhong, D. & Deng, W. (2003). Cenozoic volcanism in Tibet: evidence from a transition from oceanic to continental subduction. *Journal of Petrology* **44**, 1833–1865.

Dong, X., Zhang, Z. M., Geng, G. S., Liu, F., Wang, W. & Yu, F. (2010*a*). Devonian magmatism from the southern Lhasa terrane, Tibetan Plateau. *Acta Petrologica Sinica* **26**, 2226–2232 (in Chinese with English abstract).

Dong, X., Zhang, Z. M. & Santosh, M. (2010*b*). Zircon U–Pb chronology of the Nyingtri Group, southern Lhasa terrane, Tibetan Plateau: implications for Grenvillian and Pan-African provenance and Mesozoic–Cenozoic metamorphism. *Journal of Geology* **118**, 677–690.

Dong, X., Zhang, Z. M., Liu, F., Wang, W., Yu, F. & Shen, K. (2011*a*). Zircon U–Pb geochronology of the Nyainqêntanglha Group from the Lhasa terrane: New constraints on the Triassic orogeny of the south Tibet. *Journal of Asian Earth Sciences* **42**, 723–739.

Dong, X., Zhang, Z. M., Santosh, M., Wang, W., Yu, F. & Liu, F. (2011*b*). Late Neoproterozoic thermal events in the northern Lhasa terrane, south Tibet: Zircon chronology and tectonic implications. *Journal of Geodynamics* **52**, 389–405.

Ellis, D. J. (1987). Origin and evolution of granulites in normal and thickened crust. *Geology* **15**, 167–170.

Fuhrman, M. L. & Lindsley, D. H. (1988). Ternary-feldspar modeling and thermometry. *American Mineralogist* **73**, 201–215.

Gaidies, F., Abart, R., Capitani, C. D. E., Schuster, R., Connolly, J. A. D. & Reusser, E. (2006). Characterization of polymetamorphism in the Austroalpine basement east of the Tauern Window using garnet isopleth thermobarometry. *Journal of Metamorphic Geology* **24**, 451–475.

Garrido, C. J., Bodinier, J. L., Burg, J. P., Zeilinger, G., Hussain, S. S., Dawood, H., Chaudhry, M. N. & Gervilla, F. (2006). Petrogenesis of mafic garnet granulite in the lower crust of the Kohistan Paleo-arc Complex (Northern Pakistan): implications for intra-crustal differentiation of island arcs and generation of continental crust. *Journal of Petrology* **47**, 1873–1914.

Garrido, C. J., Bodinier, J. L., Dhuime, B., Bosch, D., Chanefo, I., Bruguier, O., Hussain, S. S., Dawood, H. & Burg, J. P. (2007). Origin of the island arc Moho transition zone via melt–rock reaction and its implications for intracrustal differentiation of island arcs: Evidence from the Jijal complex (Kohistan complex, northern Pakistan). *Geology* **35**, 683–686.

Gehrels, G., Kapp, P., DeCelles, P., Pullen, A., Blakey, R., Weislogel, A., Ding, L., Guynn, J., Martin, A., McQuarrie, N. & Yin, A. (2011). Detrital zircon geochronology of pre-Tertiary strata in the Tibetan–Himalayan orogen. *Tectonics* **30**, TC5016, http://dx.doi.org/10.1029/2011TC002868.

Gibson, G. M., McDougall, I. & Ireland, T. R. (1988). Age constraints on metamorphism and development of a metamorphic core complex in Fiordland, southern New Zealand. *Geology* **16**, 405–408.

Green, E., Holland, T. & Powell, R. (2007). An order–disorder model for omphacitic pyroxenes in the system jadeite–diopside–hedenbergite–acmite, with applications to eclogitic rocks. *American Mineralogist* **92**, 1181–1189.

Guo, L., Zhang, H.-F., Harris, N., Pan, F.-B. & Xu, W.-C. (2011). Origin and evolution of multi-stage felsic melts in eastern Gangdese belt: Constraints from U–Pb zircon dating and Hf isotopic composition. *Lithos* **127**, 54–67.

Guo, L., Zhang, H. F., Harris, N., Parrish, R., Xu, W. C. & Shi, Z. L. (2012). Paleogene crustal anatexis and metamorphism in Lhasa terrane, eastern Himalayan syntaxis: Evidence from U–Pb zircon ages and Hf isotopic compositions of the Nyingchi Complex. *Gondwana Research* **21**, 100–111.

Harley, S. L. (1989). The origins of granulites: a metamorphic perspective. *Geological Magazine* **126**, 215–247.

Harris, N. B. W., Holland, T. J. B. & Tindle, A. G. (1988). Metamorphic rocks of the 1985 Tibet Geotraverse, Lhasa to Golmud. *Philosophical Transactions of the Royal Society of London, Series A* **327**, 203–213.

Hebert, R., Bezard, R., Guilmette, C., Dostal, J., Wang, C. S. & Liu, Z. F. (2012). The Indus–Yarlung Zangbo ophiolites from Nanga Parbat to Namche Barwa syntaxes, southern Tibet: First synthesis of petrology, geochemistry and geochronology within incidences on geodynamic reconstructions of Neo-Tethys. *Gondwana Research* **22**, 377–397.

Heuberger, S., Schaltegger, U., Burg, J. P., Villa, I. M., Frank, M., Dawood, H., Hussain, S. & Zanchi, A. (2007). Age and isotopic constraints on magmatism along the Karakoram–Kohistan Suture Zone, NW Pakistan: evidence for subduction and continued convergence after India–Asia collision. *Swiss Journal of Geosciences* **100**, 85–107.

Hildreth, W. & Moorbath, S. (1988). Crustal contributions to arc magmatism in the Andes of Central Chile. *Contributions to Mineralogy and Petrology* **98**, 455–489.

Holland, T. J. B. & Powell, R. (1998). An internally consistent thermodynamic data set for phases of petrological interest. *Journal of Metamorphic Geology* **16**, 309–343.

Hollis, J. A., Clarke, G. L., Klepeis, K. A., Daczko, N. R. & Ireland, T. R. (2003). Geochronology and geochemistry of high-pressure granulites of the Arthur River Complex, Fiordland, New Zealand: Cretaceous magmatism and metamorphism on the paleo-Pacific Margin. *Journal of Metamorphic Geology* **21**, 299–313.

Hollis, J. A., Clarke, G. L., Klepeis, K. A., Daczko, N. R. & Ireland, T. R. (2004). The regional significance of Cretaceous magmatism and metamorphism in Fiordland, New Zealand, from U–Pb zircon geochronology. *Journal of Metamorphic Geology* **22**, 604–627.

Honegger, K., Dietrich, V., Frank, W., Gansser, A., Thoni, M. & Trommsdorf, V. (1982). Magmatism and metamorphism in the Ladakh Himalayas (the Indus Tsangpo Suture Zone). *Earth and Planetary Science Letters* **60**, 253–292.

Hou, Z. Q. & Cook, N. J. (2009). Metallogenesis of the Tibetan collisional orogen: A review and introduction to the special issue. *Ore Geology Reviews* **36**, 2–24.

Hou, Z. Q., Gao, Y. F., Qu, X. M., Rui, Z. Y. & Mo, X. X. (2004). Origin of adakitic intrusives generated during mid-Miocene east–west extension in southern Tibet. *Earth and Planetary Science Letters* **220**, 139–155.

Hu, Z. C., Gao, S., Liu, Y. S., Hu, S. H., Chen, H. H. & Yuan, H. L. (2008). Signal enhancement in laser ablation ICP-MS by addition

of nitrogen in the central channel gas. *Journal of Analytical Atomic Spectrometry* **23**, 1093–1101.

Hu, Z. C., Liu, Y. S., Chen, L., Zhou, L., Li, M., Zong, K. Q., Zhu, L. & Gao, S. (2011). Contrasting matrix induced elemental fractionation in NIST SRM and rock glasses during laser ablation ICP-MS analysis at high spatial resolution. *Journal of Analytical Atomic Spectrometry* **26**, 425–430.

Hu, Z. C., Liu, Y. S., Gao, S., Liu, W. G., Zhang, W., Tong, X. R., Lin, L., Zong, K. Q., Li, M., Chen, H. H., Zhou, L. & Yang, L. (2012). Improved *in situ* Hf isotope ratio analysis of zircon using newly designed X skimmer cone and jet sample cone in combination with the addition of nitrogen by laser ablation multiple collector ICP-MS. *Journal of Analytical Atomic Spectrometry* **27**, 1391–1399.

Hyndman, R. D., Currie, C. A. & Mazzotti, S. P. (2005). Subduction zone backarcs, mobile belts, and orogenic heat. *GSA Today* **15**, 4–10.

Jagoutz, O. & Schmidt, M. W. (2012). The formation and bulk composition of modern juvenile continental crust: The Kohistan arc. *Chemical Geology* **298–299**, 79–96.

Jagoutz, O., Müntener, O., Burg, J.-P., Ulmer, P. & Jagoutz, E. (2006). Lower continental crust formation through focused flow in km-scale melt conduits: the zoned ultramafic bodies of the Chilas Complex in the Kohistan Island arc (NW Pakistan). *Earth and Planetary Science Letters* **242**, 320–342.

Jagoutz, O., Muntener, O., Ulmer, P., Pettke, T., Burg, J. P., Dawood, H. & Hussain, S. (2007). Petrology and mineral chemistry of lower crustal intrusions: the Chilas Complex, Kohistan (NW Pakistan). *Journal of Petrology* **48(10)**, 1895–1953.

Jagoutz, O. E., Burg, J. P., Hussain, S., Dawood, H., Pettke, T., Iizuka, T. & Maruyama, S. (2009). Construction of the granitoid crust of an island arc part I: geochronological and geochemical constraints from the plutonic Kohistan (NW Pakistan). *Contributions to Mineralogy and Petrology* **158**, 739–755.

Jagoutz, O., Muentener, O., Schmidt, M. W. & Burg, J. P. (2011). The roles of flux- and decompression melting and their respective fractionation lines for continental crust formation: Evidence from the Kohistan arc. *Earth and Planetary Science Letters* **303**, 25–36.

Jagoutz, O. E. (2010). Construction of the granitoid crust of an island arc. Part II: a quantitative petrogenetic model. *Contributions to Mineralogy and Petrology* **160**, 359–381.

Ji, W. Q., Wu, F. Y., Chung, S. L., Li, J. X. & Liu, C. Z. (2009). Zircon U–Pb geochronology and Hf isotopic constraints on petrogenesis of the Gangdese batholith, southern Tibet. *Chemical Geology* **262**, 229–245.

Ji, W. Q., Wu, F. Y., Liu, C. Z. & Chung, S. L. (2012). Identification of early Carboniferous granitoids from southern Tibet and implications for terrane assembly related to the Paleo-Tethyan evolution. *Journal of Geology* **120**, 531–541.

Kapp, J. L. D., Harrison, T. M., Kapp, P., Grove, M., Lovera, O. M. & Ding, L. (2005*b*). Nyainqentanglha Shan: a window into the tectonic, thermal, and geochemical evolution of the Lhasa block, southern Tibet. *Journal of Geophysics Research* **110**, B08413, doi:10.1029/2004JB003330.

Kapp, P., DeCelles, P. G., Leier, A. L., Fabijanic, J. M., He, S., Pullen, A. & Gehrels, G. E. (2007). The Gangdese retroarc thrust belt revealed. *GSA Today* **17**, 4–9.

Kapp, P., Yin, A., Harrison, T. M. & Ding, L. (2005*a*). Cretaceous–Tertiary shortening, basin development, and volcanism in central Tibet. *Geological Society of American Bulletin* **117**, 865–878.

Kay, S. M. & Mpodozis, C. (2002). Magmatism as a probe to the Neogene shallowing of the Nazca plate beneath the modern Chilean flat-slab. *Journal of South American Earth Sciences* **15**, 39–57.

Kemp, A. I. S., Shimura, T. & Hawkesworth, C. J. & Edinburgh Ion Microprobe Facility (2007). Linking granulites, silicic magmatism, and crustal growth in arcs: Ion microprobe (zircon) U–Pb ages from the Hidaka metamorphic belt. *Geology* **35**, 807–810.

Khan, M. A., Treloar, P. J., Khan, M. A., Khan, T., Qazi, M. S. & Jan, M. Q. (1998). Geology of the Chalt–Babusar transect, Kohistan terrane, N. Pakistan: implications for the constitution and thickening of island-arc crust. *Journal of Asian Earth Sciences* **16**, 253–268.

Kinny, P. D. & Maas, R. (2003). Lu–Hf and Sm–Nd isotope systems in zircon. In: Hanchar, J. M. & Hoskin, P. W. O. (eds) *Zircon. Mineralogical Society of America and Geochemical Society, Reviews in Mineralogy and Geochemistry* **53**, 327–341.

Klepeis, K. A., King, D., de Paoli, M., Clarke, G. L. & Gehrels, G. (2007). Interaction of strong lower and weak middle crust during lithospheric extension in western New Zealand. *Tectonics* **26**, TC4017, doi:10.1029/2006TC002003.

Lee, H. Y., Chung, S. L., Lo, C. H., JI, J. Q., Lee, T. Y., Qian, Q. & Zhang, Q. (2009). Eocene Neotethyan slab breakoff in southern Tibet inferred from the Linzizong volcanic record. *Tectonophysics* **477**, 20–35.

Liu, Y. S., Hu, Z. C., Gao, S., Günther, D., Xu, J., Gao, C. G. & Chen, H. H. (2008). *In situ* analysis of major and trace elements of anhydrous minerals by LA-ICP-MS without applying an internal standard. *Chemical Geology* **257**, 34–43.

Liu, Y. S., Gao, S., Hu, Z., Gao, C., Zong, K. & Wang, D. (2010). Continental and oceanic crust recycling-induced melt–peridotite interactions in the Trans-North China Orogen: U–Pb dating, Hf isotopes and trace elements in zircons of mantle xenoliths. *Journal of Petrology* **51**, 537–571.

Ludwig, K. R. (2003). *ISOPLOT 3.00: A Geochronological Toolkit for Microsoft Excel. Berkeley Geochronology Center, Special Publications* **1a**.

Middlemost, E. A. K. (1994). Naming materials in the magma/igneous rock system. *Earth-Science Reviews* **37**, 215–224.

Mo, X. X., Dong, G. C., Zhao, Z. D., Zhou, S., Wang, L. L., Qiu, R. Z. & Zhang, F. Q. (2005). Spatial and temporal distribution and characteristics of granitoids in the Gangdese, Tibet and implication for crustal growth and evolution. *Geological Journal of China University* **11**, 281–290 (in Chinese with English abstract).

Mo, X. X., Hou, Z. Q., Niu, Y. L., Dong, G. C., Qu, X. M., Zhao, Z. D. & Yang, Z. M. (2007). Mantle contributions to crustal thickening during continental collision: Evidence from Cenozoic igneous rocks in southern Tibet. *Lithos* **96**, 225–242.

Mo, X. X., Niu, Y. L., Dong, G. C., Zhao, Z. D., Hou, Z. Q., Zhou, S. & Ke, S. (2008). Contribution of syn-collisional felsic magmatism to continental crust growth: a case study of the Paleogene Linzizong volcanic succession in southern Tibet. *Chemical Geology* **250**, 49–67.

Müntener, O., Hermann, J. & Trommsdorff, V. (2000). Cooling history and exhumation of lower-crustal granulite and upper mantle (Malenco, Eastern Central Alps). *Journal of Petrology* **41**, 175–200.

Padron-Navarta, J. A., Garrido, C. J., Sanchez-Navas, A., Tommasi, A., Lopez Sanchez-Vizcaino, V., Gomez-Pugnaire, M. T. & Hussain, S. S. (2008). Oriented growth of garnet by topotactic reactions and epitaxy in high-pressure, mafic garnet granulite formed by dehydration melting of metastable hornblende-gabbronorite (Jijal Complex, Kohistan Complex, north Pakistan). *Journal of Metamorphic Geology* **26**, 855–870.

Palin, R. M., Searle, M. P., St-Onge, M. R., Waters, D. J., Roberts, N. M. W., Horstwood, M. S. A., Parrish, R. R., Weller, O., Chen, S. & Yang, J. (2013). Monazite geochronology and petrology of kyanite- and sillimanite-grade migmatites from the northwestern flank of the eastern Himalayan syntaxis. *Gondwana Research*, doi:10.1016/j.gr.2013.06.022.

Pan, F. B., Zhang, H. F., Harris, N., Xu, W. C. & Guo, L. (2012). Oligocene magmatism in the eastern margin of the east Himalayan syntaxis and its implication for the India–Asia post-collisional process. *Lithos* **154**, 182–192.

Pan, G., Ding, J., Yao, D. & Wang, L. (2004). *Geological Map of the Qinghai–Xizang (Tibet) Plateau and Adjacent Areas*. Chengdu: Chengdu Cartographic Publishing House.

Pan, G. T., Mo, X. X., Hou, Z. Q., Zhu, D. C., Wang, L. Q., Li, G. M., Zhao, Z. D., Geng, Q. R. & Liao, Z. L. (2006). Spatial–temporal framework of the Gangdese Orogenic Belt and its evolution. *Acta Petrologica Sinica* **22**, 521–533 (in Chinese with English abstract).

Pan, G. T., Wang, L. Q., Li, R. S., Yuan, S. H., Ji, W. H., Yin, F. G., Zhang, W. P. & Wang, B. D. (2012). Tectonic evolution of the Qinghai–Tibet Plateau. *Journal of Asian Earth Sciences* **53**, 3–14.

Pearce, J. A., Harris, N. B. W. & Tindle, A. G. (1984). Trace element discrimination diagrams for the tectonic interpretation of granitic rocks. *Journal of Petrology* **25**, 956–983.

Powell, R., Holland, T. & Worley, B. (1998). Calculating phase diagrams involving solid solutions via non-linear equations, with examples using THERMOCALC. *Journal of Metamorphic Geology* **16**, 577–588.

Pullen, A., Kapp, P., DeCelles, P. G., Gehrels, G. E. & Ding, L. (2011). Cenozoic anatexis and exhumation of Tethyan Sequence rocks in the Xiao Gurla Range, Southwest Tibet. *Tectonophysics* **501**, 28–40.

Ravikant, V., Wu, F. Y. & Ji, W. Q. (2009). Zircon U–Pb and Hf isotopic constraints on petrogenesis of the Cretaceous–Tertiary granites in eastern Karakoram and Ladakh, India. *Lithos* **110**, 153–166.

Ringuette, L., Martignole, J. & Windley, B. F. (1999). Magmatic crystallization, isobaric cooling, and decompression of the garnet-bearing assemblages of the Jijal Sequence (Kohistan Terrane, western Himalayas). *Geology* **27**, 139–142.

Robb, L. J., Armstrong, R. A. & Waters, D. J. (1999). The history of granulite-facies metamorphism and crustal growth from single zircon U–Pb geochronology: Namaqualand, South Africa. *Journal of Petrology* **40**, 1747–1770.

Rolland, Y., Picard, C., Pecher, A., Lapierre, H., Bosch, D. & Keller, F. (2002). The Cretaceous Ladakh arc of NW Himalaya—slab melting and melt–mantle interaction during fast northward drift of Indian plate. *Chemical Geology* **182**, 139–178.

Rubatto, D. (2002). Zircon trace element geochemistry: Partitioning with garnet and the link between U–Pb ages and metamorphism. *Chemical Geology* **184**, 123–138.

Rudnick, R. L. (1995). Making continental crust. *Nature* **378**, 571–578.

Schaltegger, U., Fanning, C. M., Gunther, D., Maurin, J. C., Schulmann, K. & Gebauer, D. (1999). Growth, annealing and recrystallization of zircon and preservation of monazite in high-grade metamorphism: conventional and *in-situ* U–Pb isotope, cathodoluminescence and microchemical evidence. *Contributions to Mineralogy and Petrology* **134**, 186–201.

Schaltegger, U., Zeilinger, G., Frank, M. & Burg, J.-P. (2002). Multiple mantle sources during island arc magmatism: U–Pb and Hf isotopic evidence from the Kohistan arc complex, Pakistan. *Terra Nova* **14**, 461–468.

Schärer, U., Xu, R. H. & Allègre, C. J. (1984). U–Pb geochronology of Gangdese (Transhimalaya) plutonism in the Lhasa–Xigaze region Tibet. *Earth and Planetary Science Letters* **69**, 311–320.

Schmidt, M. W. & Poli, S. (2004). Magmatic epidote. In: Liebscher, A. & Franz, G. (eds) *Epidotes. Mineralogical Society of America and Geochemical Society, Reviews in Mineralogy and Geochemistry* **56**, 399–430.

Schubert, G. & Sandwell, D. (1989). Crustal volumes of the continents and of oceanic and continental submarine plateaus. *Earth and Planetary Science Letters* **92**, 234–246.

Scott, J. M., Copper, A. F., Palin, J. M., Tulloch, A. J., Kula, J., Jongens, R., Spell, T. L. & Pearson, N. J. (2009). Tracking the influence of a continental margin on growth of a magmatic arc, Fiordland, New Zealand, using thermobarometry, thermochronology, and zircon U–Pb and Hf isotopes. *Tectonics* **28**, TC6007, doi:10.1029/2009TC002489.

Searle, M. P., Windley, B. F., Coward, M. P., Cooper, D. J. W., Rex, D., Li, T., Xiao, X., Jan, M. Q., Thakur, V. C. & Kumar, S. (1987). The closing of Tethys and the tectonics of Himalaya. *Geological Society of American Bulletin* **98**, 678–701.

Searle, M. P., Parrish, R. R., Thow, A. V., Noble, S. R., Phillips, R. J. & Waters, D. J. (2010). Anatomy, age and evolution of a collisional mountain belt: the Baltoro granite batholith and Karakoram Metamorphic complex, Pakistani Karakoram. *Journal of the Geological Society, London* **167**, 183–202.

Searle, M. P., Elliott, J. R., Phillips, R. J. & Chung, S. L. (2011). Crustal–lithospheric structure and continental extrusion of Tibet. *Journal of the Geological Society, London* **168**, 633–672.

Shand, S. J. (1951). Eruptive rocks their genesis, composition, classification and their relation to ore-deposits with a chapter on meteorites, 4th edition. Wiley, New York, 488 p.

Singh, S., Kumar, R., Barley, M. E. & Jain, A. K. (2007). SHRIMP U–Pb ages and depth of emplacement of Ladakh batholith, eastern Ladakh, India. *Journal of Asian Earth Sciences* **30**, 490–503.

Stern, C. R. (2011). Subduction erosion: Rates, mechanisms, and its role in arc magmatism and the evolution of the continental crust and mantle. *Gondwana Research* **20**, 284–308.

Stowell, H., Tulloch, A., Zuluaga, C. & Koenig, A. (2010). Timing and duration of garnet granulite metamorphism in magmatic arc crust, Fiordland, New Zealand. *Chemical Geology* **273**, 91–110.

Tajčmanová, L., Connolly, J. & Cesare, B. (2009). A thermodynamic model for titanium and ferric iron solution in biotite. *Journal of Metamorphic Geology* **27**, 153–165.

Taylor, S. R. & McLennan, S. M. (1985). *The Continental Crust: Its Composition and Evolution*. Oxford: Blackwell.

Tinkham, D. K. & Ghent, E. D. (2005). Estimating P–T conditions of garnet growth with isochemical phase-diagram sections and the problem of effective bulk composition. *Canadian Mineralogist* **43**, 35–50.

Tulloch, A. J., Ramezani, J., Kimbrough, D. L., Faure, K. & Allibone, A. H. (2009). U–Pb geochronology of mid-Paleozoic plutonism in western New Zealand: Implications for S-type granite generation and growth of the east Gondwana margin. *Geological Society of America Bulletin* **121**, 1236–1261.

Upadhyay, R., Frisch, W. & Siebel, W. (2008). Tectonic implications of new U–Pb zircon ages of the Ladakh batholith, Indus suture zone, northwest Himalaya, India. *Terra Nova* **20**, 309–317.

Wallis, S., Tsujimori, T., Aoya, M., Kawakami, T., Terada, K., Suzuki, K. & Hyodo, H. (2003). Cenozoic and Mesozoic metamorphism in the Longmenshan orogen: Implications for geodynamic models of eastern Tibet. *Geology* **31**, 745–748.

Wang, J. L., Zhang, Z. M. & Shi, C. (2008). Anatexis and dynamics of the Lhasa terrane in the eastern Himalayan syntaxis, Tibet. *Acta Petrologica Sinica* **24**, 1539–1551 (in Chinese with English abstract).

Wei, C. J. & Song, S. G. (2008). Chloritoid–glaucophane schist in the north Qilian orogen, NW China: phase equilibria and P–T path from garnet zonation. *Journal of Metamorphic Geology* **26**, 301–316.

Weinberg, R. F. & Dunlap, W. J. (2000). Growth and deformation of the Ladakh batholith, Northwest Himalayas: implications for timing of continental collision and origin of calc-alkaline batholiths. *Journal of Geology* **108**, 303–320.

Wen, D. R., Chung, S. L., Song, B., Iizuka, Y., Yang, H. J., Ji, J., Liu, D. & Gallet, S. (2008*a*). Late Cretaceous Gangdese intrusions

of adakitic geochemical characteristics, SE Tibet: petrogenesis and tectonic implications. *Lithos* **105**, 1–11.

Wen, D. R., Liu, D. Y., Chung, S. L., Chu, M. F., Ji, J. Q., Zhang, Q., Song, B., Lee, T. Y., Yeh, M. W. & Lo, C. H. (2008*b*). Zircon SHRIMP U–Pb ages of the Gangdese batholith and implications for Neotethyan subduction in southern Tibet. *Chemical Geology* **252**, 191–201.

White, R. W., Powell, R. & Holland, T. J. B. (2007). Progress relating to calculation of partial melting equilibria for metapelites. *Journal of Metamorphic Geology* **25**, 511–527.

Whitney, D. L. & Evans, B. W. (2010). Abbreviations for names of rock-forming minerals. *American Mineralogist* **95**, 185–187.

Wiedenbeck, M., Alle, P., Corfu, F., Griffin, W. L., Meier, M., Oberli, F., Quadt, A. V., Roddick, J. C. & Spiegel, W. (1995). Three natural zircon standards for U–Th–Pb, Lu–Hf, trace element and REE analyses. *Geostandards and Geoanalytical Research* **19**, 1–23.

Wu, M. L., Zhao, G. C., Sun, M., Yin, C. Q., Li, S. Z. & Tam, P. Y. (2008). Petrology and *P–T* path of the Yishui mafic granulites: Implications for tectonothermal evolution of the Western Shandong Complex in the Eastern Block of the North China Craton. *Precambrian Research* **222–223**, 312–324.

Wu, Y. B., Gao, S., Gong, H. J., Xiang, H., Jiao, W. F., Yang, S. H., Liu, Y. S. & Yuan, H. L. (2009). Zircon U–Pb age, trace element and Hf isotope composition of Kongling terrane in the Yangtze Craton: refining the timing of Palaeoproterozoic high-grade metamorphism. *Journal of Metamorphic Geology* **27**, 461–477.

Wu, F. Y., Ji, W. Q., Liu, C. Z. & Chung, S. L. (2010). Detrital zircon U–Pb and Hf isotopic data from the Xigaze fore-arc basin: Constraints on Transhimalayan magmatic evolution in southern Tibet. *Chemical Geology* **271**, 13–25.

Xia, L. Q., Li, X. M., Ma, Z. P., Xu, X. Y. & Xia, Z. C. (2011). Cenozoic volcanism and tectonic evolution of the Tibetan plateau. *Gondwana Research* **19**, 850–866.

Xu, R. H., Schärer, U. & Allègre, C. J. (1985). Magmatism and metamorphism in the Lhasa block (Tibet): A geochronological study. *Journal of Geology* **93**, 41–57.

Xu, Z. Q., Ji, S. C., Cai, Z. H., Zeng, L. S., Geng, Q. R. & Cao, H. (2012). Kinematics and dynamics of the Namche Barwa Syntaxis, eastern Himalaya: Constraints from the deformation, fabrics and geochronology. *Gondwana Research* **21**, 19–36.

Xu, W. C., Zhang, H. F., Harris, N., Guo, L. & Pan, F. B. (2013). Rapid Eocene erosion, sedimentation and burial in the eastern Himalayan syntaxis and its geodynamic significance. *Gondwana Research* **23**, 715–725.

Yamamoto, H. (1993). Contrasting metamorphic *P–T*–time paths of the Kohistan granulites and tectonics of the western Himalayas. *Journal of Geological Society, London* **150**, 843–856.

Yamamoto, H. & Nakamura, E. (1996). Sm–Nd dating of garnet granulites from the Kohistan Complex, northern Pakistan. *Journal of Geological Society, London* **153**, 965–969.

Yamamoto, H. & Nakamura, E. (2000). Timing of magmatic and metamorphic events in the Jijal Complex of the Kohistan Arc deduced from Sm–Nd dating of mafic granulites. In: Khan, M. A., Treloar, P. J., Searle, M. P. & Jan, M. Q. (eds) *Tectonics of the Nanga Parbat Syntaxis and the Western Himalaya. Geological Society, London, Special Publications* **170**, 313–319.

Yamamoto, H. & Yoshino, T. (1998). Superposition of replacements in the mafic granulites of the Jijal complex of the Kohistan arc, northern Pakistan: dehydration and rehydration within deep arc crust. *Lithos* **43**, 219–234.

Yin, A. (2006). Cenozoic tectonic evolution of the Himalayan orogen as constrained by along-strike variation of structural geometry, exhumation history, and foreland sedimentation. *Earth-Science Reviews* **76**, 1–131.

Yin, A. & Harrison, T. M. (2000). Geologic evolution of the Himalayan Tibetan Orogen. *Annual Review of Earth and Planetary Sciences* **28**, 211–280.

Yin, G. H., Bao, G., Yang, S. S. & Hu, Q. H. (2006). The granulites and ages of the Nyingchi Group Complex in the Nyingchi region, Xizang. *Sedimentary Geology and Tethyan Geology* **26**, 8–15 (in Chinese with an English abstract).

Yoshino, T. & Okudaira, T. (2004). Crustal growth by magmatic accretion constrained by metamorphic *P–T* paths and thermal models of the Kohistan Arc, NW Himalayas. *Journal of Petrology* **45**, 2287–2302.

Yoshino, T., Yamamoto, H., Okudaira, T. & Toriumi, M. (1998). Crustal thickening of the lower crust of the Kohistan arc (N. Pakistan) deduced from Al zoning in clinopyroxene and plagioclase. *Journal of Metamorphic Geology* **16**, 729–748.

Zen, E.-A. & Hammarstrom, J. M. (1984). Magmatic epidote and its petrologic significance. *Geology* **12**, 515–518.

Zeng, L. S., Gao, L. E., Xie, K. J. & Liu-Zeng, J. (2011). Mid-Eocene high Sr/Y granites in the Northern Himalayan Gneiss Domes: Melting thickened lower continental crust. *Earth and Planetary Science Letters* **303**, 251–266.

Zhang, H. F., Xu, W. C., Guo, K. Q., Cai, H. M. & Yuan, H. L. (2007). Zircon U–Pb and Hf isotopic composition of deformed granite in the southern margin of the Gangdese belt, Tibet: evidence for early Jurassic subduction of Neo-Tethyan oceanic slab. *Acta Petrologica Sinica* **23**, 1347–1353 (in Chinese with English abstract).

Zhang, H. F., Harris, N., Guo, L. & Xu, W. C. (2009). The significance of Cenozoic magmatism from the western margin of the eastern syntaxis, southeast Tibet. *Contributions to Mineralogy and Petrology* **160**, 83–98.

Zhang, H. F., Harris, N., Guo, L. & Xu, W. C. (2010). The significance of Cenozoic magmatism from the western margin of the eastern syntaxis, southeast Tibet. *Contributions to Mineralogy and Petrology* **160**, 83–98.

Zhang, L. & Wu, Y. (2012). Origin and metamorphic evolution of the Nyingchi Complex, eastern Lhasa terrane, southern Tibet: Constraint from the zircon U–Pb geochronology. *Acta Petrologica Sinica* **28**, 1674–1688 (in Chinese with English abstract).

Zhang, Z. M. & Santosh, M. (2012). Tectonic evolution of Tibet and surrounding regions. *Gondwana Research* **21**, 1–3.

Zhang, Z. M., Zhao, G. C., Santosh, M., Wang, J. L., Dong, X. & Liou, J. G. (2010*a*). Two-stages of granulite-facies metamorphism in the eastern Himalayan syntaxis, south Tibet: Petrology, zircon geochronology and implications for the subduction of Neo-Tethys and the Indian continent beneath Asia. *Journal of Metamorphic Geology* **28**, 719–733.

Zhang, Z. M., Zhao, G. C., Santosh, M., Wang, J. L., Dong, X. & Shen, K. (2010*b*). Late Cretaceous charnockite with adakitic affinities from the Gangdese batholith, southeastern Tibet: Evidence for Neo-Tethyan mid-oceanic ridge subduction? *Gondwana Research* **17**, 615–631.

Zhang, Z. M., Dong, X., Liu, F., Lin, Y. H., Yan, R. & Santosh, M. (2012*a*). Tectonic evolution of the Amdo terrane, central Tibet: petrochemistry and zircon U–Pb geochronology. *Journal of Geology* **120**, 431–451.

Zhang, Z. M., Dong, X., Santosh, M., Liu, F., Wang, W., Yiu, F., He, Z. Y. & Shen, K. (2012*b*). Petrology and geochronology of the Namche Barwa Complex in the eastern Himalayan syntaxis, Tibet: Constraints on the origin and evolution of the north-eastern margin of the Indian Craton. *Gondwana Research* **21**, 123–137.

Zhang, Z. M., Dong, X., Santosh, M. & Zhao, G. C. (2013). Metamorphism and tectonic evolution of the Lhasa terrane, Central Tibet. *Gondwana Research*, http://dx.doi.org/10.1016/j.gr.2012.08.024.

Zhao, G. C. & Zhai, M. G. (2013). Lithotectonic elements of Precambrian basement in the North China Craton: Review and tectonic implications. *Gondwana Research* **23**, 1207–1240.

Zhao, Z. D., Mo, X. X., Dilek, Y., Niu, Y. L., DePaolo, D. J., Robinson, P., Zhu, D. C., Sun, C. G., Dong, G. C., Zhou, S., Luo, Z. H. & Hou, Z. Q. (2009). Geochemical and Sr–Nd–Pb–O isotopic compositions of the post-collisional ultrapotassic magmatism in SW Tibet: Petrogenesis and implications for India intra-continental subduction beneath southern Tibet. *Lithos* **113**, 190–212.

Zhu, D. C., Pan, G. T., Chung, S. L., Liao, Z. L., Wang, L. Q. & Li, G. M. (2008). SHRIMP zircon age and geochemical constraints on the origin of Early Jurassic volcanic rocks from the Yeba Formation, southern Gangdese in south Tibet. *International Geology Review* **50**, 442–471.

Zhu, D. C., Mo, X. X., Niu, Y. L., Zhao, Z. D., Wang, L. Q., Liu, Y. S. & Wu, F. Y. (2009*a*). Geochemical investigation of Early Cretaceous igneous rocks along an east–west traverse throughout the central Lhasa Terrane, Tibet. *Chemical Geology* **268**, 298–312.

Zhu, D. C., Mo, X. X., Niu, Y., Zhao, Z. D., Wang, L. Q., Pan, G. T. & Wu, F. Y. (2009*b*). Zircon U–Pb dating and *in-situ* Hf isotopic analysis of Permian peraluminous granite in the Lhasa terrane, southern Tibet: Implications for Permian collisional orogeny and paleogeography. *Tectonophysics* **469**, 48–60.

Zhu, D. C., Zhao, Z. D., Pan, G. T., Lee, H. Y., Kang, Z. Q., Liao, Z. L., Wang, L. Q., Li, G. M., Dong, G. C. & Liu, B. (2009*c*). Early Cretaceous subduction-related adakite-like rocks of the Gangdese Belt, southern Tibet: Products of slab melting and subsequent melt–peridotite interaction? *Journal of Asian Earth Sciences* **34**, 298–309.

Zhu, D. C., Zhao, Z. D., Niu, Y. L., Dilek, Y. & Mo, X. X. (2011*a*). Lhasa terrane in southern Tibet came from Australia. *Geology* **39**, 727–730.

Zhu, D. C., Zhao, Z. D., Niu, Y. L., Mo, X. X., Chung, S. L., Hou, Z. Q., Wang, L. Q. & Wu, F. Y. (2011*b*). The Lhasa Terrane: Record of a microcontinent and its histories of drift and growth. *Earth and Planetary Science Letters* **301**, 241–255.

Zhu, D. C., Zhao, Z. D., Niu, Y. L., Dilek, Y., Hou, Z. Q. & Mo, X. X. (2012). The origin and pre-Cenozoic evolution of the Tibetan Plateau. *Gondwana Research*, doi:10.1016/j.gr.2012.02.002.

Zong, K. Q., Liu, Y. S., Gao, C. G., Hu, Z. H., Gao, S. & Gong, H. J. (2010). *In situ* U–Pb dating and trace element analysis of zircons in thin sections of eclogite: refining constraints on the UHP metamorphism of the Sulu terrane, China. *Chemical Geology* **269**, 237–251.